Friction Models in the Solution of Nonstationary Contact Problems

KEVIN WILLIAM COLVILLE

September 1993

A dissertation submitted to the University of Cape Town in fulfillment of the requirements for the degree of Masters of Science in Applied Mathematics.

Summary

In most implementations of the finite element method for the solution of contact problems the model of friction used is the classic Amontons-Coulomb. This dissertation is an attempt to rectify the current situation by considering four more advanced friction models, and coding them in FORTRAN for use with the finite element program ABAQUS. The new models are: a quasi-steady-state sliding model proposed by Zhang, Moslehy and Rice; a nonlinear pressure-dependent model proposed by Wriggers, vu Van and Stein; and a model that includes a film of lubricant proposed by Wilson, Hsu and Huang. The friction models are described in detail, including the algorithmic implementation. The contact problem is then formulated in the Total Lagrangian and Updated Lagrangrian formulations for contact between an elastic-plastic (Mises plasticity) body and a rigid tool. The variational (weak) form of the formulation is given and this is then descretised by the finite element method. To test and compare the models three common metal forming processes are simulated: hemispherical punching of a disk, two-dimensional plane strain and three-dimensional cold rolling of a strip, and axisymmetric cup deep-drawing. The results are presented in the form of contour plots of the second invarient of stress (Mises), and the plastic yield and maximum stress. Also graphs for the thickness strain are given. These results are presented for each combination of friction model and process to allow easy comparison of frictional behavour.

Acknowledgements

I would like to thank my supervisor Dr Jacek Ronda (Dr.Sc.) for his guidance, help and patience.

I would like to thank Dr Colin Mercer for his advice on using Abaqus effectively, and his help in debugging my early efforts.

I extend thanks to Mike Eastman for helping me with any computer mishaps. I'd like to thank Graeme Oliver for clearing up the finer points of continuum mechanics for me. Thanks to Andre Bothma for allowing me to use his program for the axisymmetric cup deep drawing.

I thank Professor W.R.D. Wilson of Northweston University, Illanois, for generously sending copies of his recent work to me.

I thank Professor J.B. Martin and Professor B.D. Reddy of CERECAM for arranging funding for me which allowed me to pursue this work.

Last, but not least, I thank Mark Katz for his humour and refreshing attitude to life, the universe and academia.

Contents

Chapter 1

Introduction

In most finite element method (FEM) programs friction is implemented by the classic Amontons-Coulomb model. This has undoubtly led to a low quality of results for some contact problems, for which the conditions on the contact surface can be a significant contribution to the solution of the entire problem. In this dissertation an attempt is made to rectify the situation by considering the implementation of different friction models in a FEM package.

Four different friction models are implemented within the finite element program ABAQUS (version 5.2), which allows a user to write a FORTRAN subroutine describing the frictional stresses, sliding and other properties on a point on the contact surface between two bodies which are descretised by finite elements. The friction subroutine will be called during the analysis of the whole problem. This feature allows existing simulations to be run with different friction models with only the one subroutine requiring change.

The simulations chosen were standard "benchmark" processes: rolling, punching and deep drawing. These metal working processes all envolve large plastic deformation over a tool and would thus be dependent on frictional effects. There has been much work published on these processes and so experimental and numerical results are available ([27, 30]) to compare with the solution of a finite element simulation. Once results for a particular simulation are calculated for different friction models, they can be compared and a choice made as to which is the "best" friction model for the process. As there is yet no ideal friction model for all processes that are modelled, finding the most appropriate friction model would improve the quality of a simulation greatly. To simplify

the solution the tools were modelled as rigid bodies, and the work pieces were modeled as elastic-plastic materials.

The chosen problems were modelled within continuum mechanics using the updated Lagrangian formulation. The resulting equations of motion and boundary conditions were then cast in variational form and this could be discretised and solved numerically using the finite element method.

The finite element method is a widely used simulation tool which has proved to be successful in solving contact problems arising in metal working. Such processes involve contact between two or more bodies and include rolling, drawing, extrusion and sheet metal forming. Within sheet metal forming the main processes are stamping, stretch forming, deep drawing and ironing. All these processes involve friction, which could greatly influence the process behaviour.

Simulation of metal working problems requires the accurate modelling of the material behaviour and the interface conditions. The most difficult part of solving a contact problem is the determination of the contact surface and the stresses, forces and displacements on it. It is here that only a few papers have been published on including more realistic models of friction within the FEM. Most finite element programs utilize the classic Amontons-Coulomb model of friction.

1.1 Friction Phenomena

Research has been done in friction, both in physics (seeking the basic mechanisms) [3, 4, 31] and engineering (quantifying the effects on processes), and on the associated phenomena of abrasion and wear [14, 29]. Work has also been done on evaluating and describing the real surface of contact. This information, particularly mathematical models of friction, can be used to include new models of friction within the FEM.

By friction we mean the resistance to tangential motion experienced by two bodies in contact. We are concerned with describing this resistance as frictional forces or stresses on the contact surface. We also consider how this affects the

relative tangential motion (sliding) on the contact surface. We will not consider the phenomena of wear.

Friction consists of several phenomena which contribute to the total frictional resistance. These will be mentioned briefly here, and those phenomena which are incorperated into the friction models studied will be described in detail in chapter 2.

Real surfaces are not smooth, but consist of asperities and valleys on the microscopic scale. The asperities are the main contributors to friction. When two surfaces come into contact this will occur on the peaks of asperities. As contact appears on isolated points, not over the whole surface, the real contact area will differ from the nominal contact area [14].

Adhesion takes place owing to the natural molecular attraction from van der Waals forces or chemical bonding, or from microwelds as a result of the high pressures which develop over the small contact area between asperities. Adhesion depends on the strength of the bond and on the area of bonding. Friction would then arise from the stress needed to break a bond.

Asperities can interlock if the peak of one asperity lies in the valley of the other surface. This means that sliding could only occur if the asperities shear. Asperities that have bonded could also shear rather than break the bond. Thus, friction would arise from the shear strength of the materials.

Rather than shear, interlocking asperities could plough into the base material, deforming the shape of the surface. Then friction would arise from the work needed to deform the material plastically. Plowing and shearing would also result in separate pieces of material being deposited between the contacting surfaces. As this debris is usually much harder than the parent material owing to oxidation and/or work hardening, the debris contributes by ploughing into the main bodies. Friction then arises from surface cutting, plastic deformation and fracture.

The contacting asperities could deform into flatter shapes, smoothing the surfaces. This friction would result from elastic and plastic deformation of the asperities. A consequence of this is that the topology of the surface changes, affecting the real contact area and material properties.

The above description assumes that there is no lubricant between surfaces. The presence of a lubricant complicates matters as the behaviour of the lubricant must be considered. In the case of a liquid lubricant we can model it using fluid dynamics provided the lubricant film is thick enough [7].

When the lubricant is thick enough to completely separate the surfaces so that there is no contact between asperities, then friction will be due to viscous shear within the fluid. The case when surface roughness effects are negligible is known as **thick film** lubrication. The case when the two surfaces are still completely separated, and the surface roughness effects are no longer small, the friction is due to viscous shear, and this must be modified to account for the contribution of roughness. This is usually due to the change in fluid velocity near the asperities. This is known as **thin film** lubrication.

Should the lubricant be thin enough to allow asperity contacts, the phenomena described for dry friction will operate, as well as the fluid shear. Lubricant will tend to be trapped in valleys in the surfaces, and so limit the contact area from expanding under increasing pressure as the entrapped pools of lubricant support the normal load. A very thin bounday layer of lubricant will exist between some of the asperity contacts, and others will be dry. This is known as **mixed film** lubrication. The frictional stress is now composed of the contributions from viscous shear in the pools of entrapped lubricant, the shear strength of the boundary film, and the frictional stress of the areas in dry contact.

When the film is very thin (a few molecules thick) and merely coats the surface asperities, there will be no pools of entrapped lubricant. Then the dry frictional phenomena will act along with the effect of the thin boundary film. This case is known as **boundary film** lubrication.

More advanced friction models have been proposed which take into account the above phenomena. These more realistic models consider the individual contribution of each separate interaction.

1.2 Friction and the Finite Element Method

The frictional contact problem is formulated as a minimisation problem, which is solved numerically by the FEM. Such a simulation of contact requires that the FEM include procedures and algorithms for determining: when and where contact occurs, the conditions of contact (stresses, displacements), and friction and other interface contributions (wear). Two approaches are used to include the contact constraints: Lagrange multipliers and penalty function methods. As contact algorithms are not the concern of this report, it was decided to use an existing FEM package which can simulate contact problems. The FEM program ABAQUS was chosen, which uses a Lagrange multiplier method.

Four models of friction will be presented in this dissertation. Each model is coded in FORTRAN and implemented within ABAQUS. The models are tested by using each to solve a metal forming simulation. The results are compared in order to select the most appropriate model for a particular manufacturing process.

The most successful approach to incorperating friction within the FEM is the "plasticity" theory of friction, which was proposed by Friedriksson, and also Michalowski and Mroz, and Curnier (see [9, 21]). This theory constructs an analogy between friction and plasticity from the following similarities:

Friction	Plasticity
Decomposition of sliding into stick and slip	Decomposition of strain into elastic and plastic parts
Laws of stick and wear	Laws of elastic, kinematic and isotropic hardening
A slip criterion	A yield criterian
Slip rules	Yield rules

The stick state of friction is comparable to the elastic state of elasto-plasticity as any displacement which occurs during sticking is owing to the elastic deformation of asperities. Similarly the slip state of friction is due partly to plastic deformation of asperities (and also debris particles, if present) and mostly due to the breaking of the bonds formed between contacting asperities.

The theory for the plasticity approach to friction will be presented in chapter 2, along with the algorithms used. The algorithm that results from this approach is quite general, and can accomodate different models of friction which consider pressure, temperature, work hardening and wear effects on the frictional stresses. The further advantage of this approach is that the numerical integration algorithms developed for plasticity can be used.

Most implementations of friction within the FEM have used the Coulomb model. Extensive work was done by Oden and Pires [16, 17, 18] and Kikuchi [13] within elasticity on nonlinear and nonlocal dry models of friction. However, these models have not proved as useful for simulating real contact. Nonlocal friction models have not been considered in this report because it was not possible to implement such a model within ABAQUS which only provides local information to the friction subroutine. Other models of dry friction have been implemented by Wriggers, et al. [40], Peric and Owen [21], Rodic and Owen [23] and Buczkowski and Klieber [6]. All these have used a version of the plasticity approach, coupled with empirical or theoretical relations for the frictional stresses and displacements. In chapter 2 a theoretical model of friction due to Zhang, et al. [41, 42] is incorperated within the FEM using the plasticity approach. It is thus possible to easily include new models of friction. For example, a new friction model which takes accounts the wear of the surface of coated steels by using a "work-hardening" law [22].

Friction models with lubrication have been implemented within the FEM by Wilson, et al. [36, 38]. These models are more recent and there are few other FEM implementations of lubricated friction. In chapter 2 the Wilson model is described and implemented for two dimensional axisymmetric processes.

Chapter 2

Friction Models

Four friction models were selected for comparison.

1. The classic Amontons-Coulomb (AC) model of friction is the most frequently used model in both theoretical and numerical analysis of contact problems. It is thus chosen as the "benchmark" model against which the others are judged. The popularity of this model stems from its simplicity and also its usefulness for predicting real friction. However, the model is insufficient in many of the problems studied today, particularly the metal forming processes with large surface motion and the most common situation of lubricated surfaces.

2. A logical improvement on the AC model is a nonlinear pressure dependent model (WVS) described by Wriggers, vu Van & Stein, which is chosen because, while more complicated than AC, it is still fairly simple and, moreover, it is based on realistic well-measured phenomena.

3. The above models do not differentiate between the cases of non-sliding and sliding contact, assuming that the frictional stress stays the same. Thus a quasi-steady-state sliding friction model (QSS) is examined to describe friction during sliding.

4. As most contact situations are not dry, a lubricated friction model is used. This model is the most complicated as the introduction of a film

of lubrication gives rise to more states of frictional contact than the stick-sliding states of dry models.

These four friction models are described here in detail.

2.1 Amontons-Coulomb Model

The most frequently used friction model is one proposed initially by Amontons (1699) based on experimental work and later extended by Coulomb (1781) (see [13, §1.3] and [14, p.158]). The model is described by

$$\|\mathbf{t}_T\| = \mu|t_N| = \mu|p| \tag{2.1}$$

where: $\mathbf{t}_T$ is the tangental or frictional stress,
t_N is the normal stress,
p is the pressure, and
μ is the coefficient of friction.

For the classic Amontons-Coulomb model μ is a real constant which depends on material parameters and the surface condition, but it also can be a function of state variables such as pressure, temperature, velocity, etc. In the latter case we are in the regime of more advanced friction models.

In order to use this model within the FEM it is necessary to develop an algorithm which will update the variables on the contact surface for each FEM time increment. The approach used is to numerically integrate the plasticity theory of friction described in chapter 1. This is done below.

For the numerical implementation of the Amontons-Coulomb model we use the geometry of figure 2.1. The displacement on the surface is separated into the normal h and the two tangental displacements u_1, u_2. Similarly the frictional stresses are separated into the normal stress p, which is just the pressure, and the tangental stresses t_1, t_2.

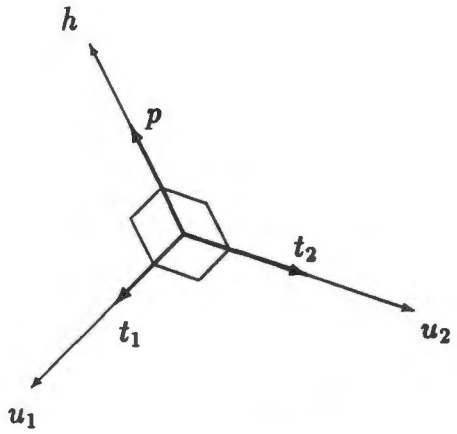

Figure 2.1: Directions of the displacement and stress components used for friction.

Dry frictional contact has been observed to have two states: stick and slip. In the stick state there is no or little relative motion between the contacting surfaces. In the slip state large relative motion occurs as the two bodies slide against each other. Thus it is necessary to assume a rate decomposition of the tangental relative motion

$$\dot{\mathbf{u}} = \dot{\mathbf{u}}^{\mathrm{el}} + \dot{\mathbf{u}}^{\mathrm{sl}} \tag{2.2}$$

where 'el' denotes elastic stick part and 'sl' denotes slip part. Now it has been observed that the stick state is not perfect stick with no slip, instead microsliding occurs before the surfaces slip. In Kragelsky, et al. [14, fig. 5.2] and Bowden & Tabor [4] the stick state is shown as elastic, i.e. the friction stress depends on the relative displacement. Hence we will adopt "elastic stick" for the non-slipping state.

Assume elastic stick is linear with a stiffness constant of g, then in a state of stick, the frictional stress is just

$$\mathbf{t} = g\mathbf{u}^{\mathrm{el}} \tag{2.3}$$

$$\mathbf{u}^{\mathrm{el}} = \sum \Delta \mathbf{u}^{\mathrm{el}} \tag{2.4}$$

for the current time increment, where the summation is taken over all previous time increments.

In order to implement the friction model in algorithmic form, the friction model is described in an analogy to plasticity. This uses a yield function that determines which state the friction is in, and a flow rule for the case of sliding (slipping).

Define the AC yield function as

$$f = \|\mathbf{t}\| - \mu p \tag{2.5}$$

where $\|\cdot\|$ is the Euclidean norm, i.e. $\|\mathbf{t}\| = \sqrt{\mathbf{t}\cdot\mathbf{t}}$. Then if $f \leq 0$ at the end of the increment, assuming $\Delta\mathbf{u}^{\mathrm{sl}} = 0$ during the increment, there is no slip. Otherwise slip occurs according to the associated flow rule

$$\dot{\mathbf{u}}^{\mathrm{sl}} = \dot{\gamma}\frac{\partial f}{\partial \mathbf{t}} = \dot{\gamma}\frac{\mathbf{t}}{\|\mathbf{t}\|} \tag{2.6}$$

where γ is a real function.

Equations (2.3), (2.5) and (2.6) are a complete description of the friction model. However, in order to use it we must solve the relations to obtain the current frictional stress and slip.

Integrate the tangental displacement rate decomposition (2.2) over a time increment Δt so that

$$\Delta\mathbf{u} = \Delta\mathbf{u}^{\mathrm{el}} + \Delta\mathbf{u}^{\mathrm{sl}}, \tag{2.7}$$

$$\Delta\mathbf{u}^{\mathrm{sl}} = \Delta\gamma\frac{\mathbf{t}}{\|\mathbf{t}\|}. \tag{2.8}$$

At the end of the current time increment i the frictional stress is

$$\begin{aligned}
\mathbf{t}_i &= g\mathbf{u}_i^{\mathrm{el}} = g(\mathbf{u}_i - \mathbf{u}_i^{\mathrm{sl}}) \\
&= g\left[\mathbf{u}_i - (\mathbf{u}_{i-1}^{\mathrm{sl}} + \Delta\mathbf{u}_i^{\mathrm{sl}})\right] \\
&= g(\mathbf{u}_i - \mathbf{u}_{i-1}^{\mathrm{sl}}) - g\Delta\mathbf{u}_i^{\mathrm{sl}} \\
&= \mathbf{t}_i^{\mathrm{el}} - g\Delta\mathbf{u}_i^{\mathrm{sl}}
\end{aligned} \tag{2.9}$$

where $\mathbf{t}_i^{\mathrm{el}}$ is the value of $\mathbf{t}_i$ if there is *no* slip during the increment.

Unless otherwise indicated all variables refer to the current increment and the subscript i is omitted from now on. So now we have

$$\begin{aligned} \mathbf{t} &= \mathbf{t}^{\mathrm{el}} - g\Delta\mathbf{u}^{\mathrm{sl}} \\ \Rightarrow \quad \Delta\mathbf{u}^{\mathrm{sl}} &= (\mathbf{t}^{\mathrm{el}} - \mathbf{t})/g. \end{aligned} \tag{2.10}$$

Substitute the flow rule equation (2.8) into equation (2.10)

$$\Delta\gamma\frac{\mathbf{t}}{\|\mathbf{t}\|} = \frac{\mathbf{t}^{\mathrm{el}}}{g} - \frac{\mathbf{t}}{g}$$

and solve for $\mathbf{t}$ to obtain

$$\begin{aligned} \mathbf{t} &= \mathbf{t}^{\mathrm{el}} \Big/ g\left(\frac{\Delta\gamma}{\|\mathbf{t}\|} + \frac{1}{g}\right) \\ &= \mathbf{t}^{\mathrm{el}} \Big/ \left(1 + \Delta\gamma\frac{g}{\|\mathbf{t}\|}\right). \end{aligned} \tag{2.11}$$

Calculate the magnitude of $\mathbf{t}$ from the imposed yield condition $\|\mathbf{t}\| - \mu p = 0$, and substitute this into equation (2.11) to obtain the magnitude of the frictional sticking stress

$$\begin{aligned} \|\mathbf{t}^{\mathrm{el}}\| &= \mu p\left(1 + \Delta\gamma\frac{g}{\mu p}\right) \\ &= \mu p + g\Delta\gamma \end{aligned}$$

and the increment of function γ

$$\Delta\gamma = (\|\mathbf{t}^{\mathrm{el}}\| - \mu p)/g \tag{2.12}$$

Now substitute this back into equation (2.11) to obtain the tangental stress

$$\begin{aligned} \mathbf{t} &= \mathbf{t}^{\mathrm{el}} \Big/ \left(1 + \frac{\|\mathbf{t}^{\mathrm{el}}\| - \mu p}{g}\frac{g}{\mu p}\right) \\ &= \mu p\frac{\mathbf{t}^{\mathrm{el}}}{\|\mathbf{t}^{\mathrm{el}}\|} \end{aligned} \tag{2.13}$$

and substitute into equation (2.8) to obtain the increment in slip

$$\begin{aligned} \Delta\mathbf{u}^{\mathrm{sl}} &= \left(\frac{\|\mathbf{t}^{\mathrm{el}}\| - \mu p}{g}\right)\left(\mu p\frac{\mathbf{t}^{\mathrm{el}}}{\|\mathbf{t}^{\mathrm{el}}\|}\right) \Big/ \mu p \\ &= \frac{\|\mathbf{t}^{\mathrm{el}}\| - \mu p}{g}\frac{\mathbf{t}^{\mathrm{el}}}{\|\mathbf{t}^{\mathrm{el}}\|} \end{aligned} \tag{2.14}$$

The algorithm for the implementation of the friction model is thus

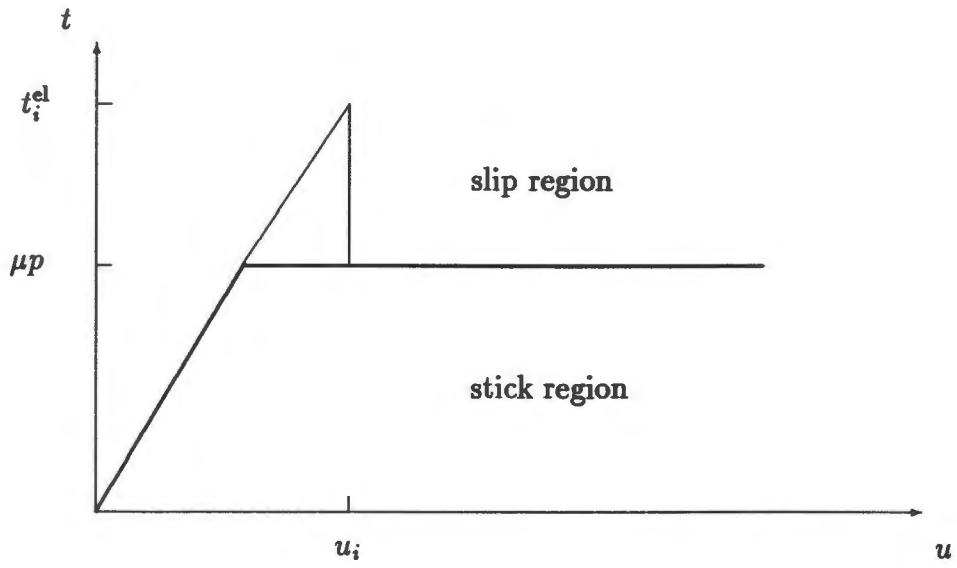

Figure 2.2: Graph showing how the elastic predictor step is corrected for the slip region.

input t_{i-1}, $\Delta\mathrm{u}_i$, p
initialize calculate elastic predictor
  $\mathrm{t}^{\mathrm{el}} \leftarrow \mathrm{t}_{i-1} - g\Delta\mathrm{u}_i$
  $t^{\mathrm{el}} \leftarrow \sqrt{\mathrm{t}^{\mathrm{el}} \cdot \mathrm{t}^{\mathrm{el}}}$
  $f \leftarrow t^{\mathrm{el}} - \mu p$
if $f \leq 0$
  then elastic stick state
    $\mathrm{t}_i \leftarrow \mathrm{t}^{\mathrm{el}}$
    $\Delta\mathrm{u}_i^{\mathrm{sl}} \leftarrow 0$
    $\partial\mathrm{t}/\partial p \leftarrow 0$
    $\partial\mathrm{t}/\partial\mathrm{u} \leftarrow -gI$
  else slip state
    $\mathrm{t}_i \leftarrow \mu p(\mathrm{t}^{\mathrm{el}}/t^{\mathrm{el}})$
    $\Delta\mathrm{u}_i^{\mathrm{sl}} \leftarrow ([\mu p - t^{\mathrm{el}}]/g)(\mathrm{t}^{\mathrm{el}}/t^{\mathrm{el}})$
    $\partial\mathrm{t}/\partial p \leftarrow \mu$
    $\partial\mathrm{t}/\partial\mathrm{u} \leftarrow 0$
output t_i, $\Delta\mathrm{u}_i^{\mathrm{sl}}$, $\partial\mathrm{t}/\partial p$, $\partial\mathrm{t}/\partial\mathrm{u}$
return

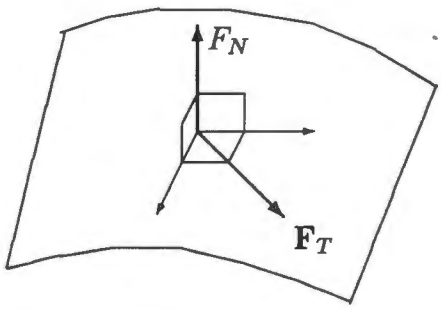

Figure 2.3: The directions on the contact surface for the WVS model.

The algorithm is similar to the radial return algorithms used in plasticity. It would be implemented within a finite element method program, and would provide the program with the frictional stress and slip calculations. Figure 2.2 illustrates how the predicted elastic friction stress is corrected to the friction yield limit when $f > 0$. The amount of slip is then calculated. The reason that the derivatives $\partial \mathbf{t}/\partial p$ and $\partial \mathbf{t}/\partial \mathbf{u}$ are also calculated is to provide these for the Jacobian in the FEM solution. This arises from the consistent linearisation of the state variables. The most important feature of the algorithm here is that it is general enough to include other models of friction. Including analogues of work-hardening to account for the effects of wear on a surface.

2.2 Wriggers, vu Van and Stein Model

Wriggers, vu Van and Stein have proposed a friction model for use within finite element analysis with a nonlinear relation between the frictional yield function and the normal force between surfaces [39]. The model is based on work described by Kragelski, et al. [14]. The force acting on the surface is separated into the tangental and normal components, as in figure 2.3. Here we consider the surface forces rather than the surface stresses as in the AC model.

The model consists of two empirical relationships. The first is between nominal and real contact areas. The expression given by Woo and Thomas [38] is used:

$$\frac{A_r}{A} = \left(\frac{|F_N|}{AH}\right)^{\nu} \tag{2.15}$$

where: A_r is the real area of contact,
A is the nominal area of contact,
H is the surface hardness,
F_N is the normal force between surfaces, and
ν is a parameter $(0 < \nu \leq 1)$.

The second relation in the model is between the shear stress and the contact pressure [14]:

$$t = t_0 + \beta p_r \tag{2.16}$$

where: t_0 and β are constants and
p_r is the actual contact pressure.

The contact pressure p_r is defined by the relation to the normal force F_N and the real area of contact A_r

$$\begin{aligned} p_r &= \frac{|F_N|}{A_r} = |F_N| \Big/ A \left(\frac{|F_N|}{AH}\right)^{\nu} \\ &= \left(\frac{|F_N|}{A}\right)^{1-\nu} H^{\nu} \end{aligned} \tag{2.17}$$

and the magnitude of tangental force $\mathbf{F}_T$ is

$$\begin{aligned} \|\mathbf{F}_T\| &= A_r t_r = (t_0 + \beta p_r) A_r \\ &= \alpha |F_N|^{\nu} + \beta |F_N| \end{aligned} \tag{2.18}$$

where

$$\alpha = \frac{A t_0}{(AH)^{\nu}}. \tag{2.19}$$

And we define, similarly to the AC model equation (2.5), a frictional yield function

$$f = \|\mathbf{F}_T\| - \alpha |F_N|^{\nu} - \beta |F_N|. \tag{2.20}$$

This function differs from equation (2.5) by the new nonlinear term $\alpha|F_N|^\nu$.

Using the same flow rule (2.6) gives essentially the same algorithm except for the new nonlinear expression for the yield frictional stress. Hence, the same algorithm is used for the WVS model as for the AC model, with the expression μp replaced by $\alpha p^\nu + \beta p$. Note that we use stresses in the algorithm; they are obtained by dividing the forces $\mathbf{F}_T$ and F_N by the real area of contact A_r.

2.3 Quasi-steady-state Sliding Model

As described in the introduction, friction depends on several phenomena, which need to be mathematically modelled in order to accurately predict the value of the friction coefficient of a tribosystem.

Zhang, Moslehy & Rice have considered this in [41] assuming that the contact between the surfaces is quasi-steady-state sliding. That is, the two surfaces are sliding but the contact parameters (e.g., real area of contact, asperity heights, hardness, etc.) are constant, hence "steady-state". But such a situation is not realistic, hence "quasi-". To explain what quasi-steady-state sliding is we quote [41].

"After sliding begins, friction results in plastic deformation near the interface between interacting materials. Heat is produced during deformation and during subsequent recovery processes. This frictional heat raises the temperature of the friction couple and this leads to changes in material properties such as work hardening and recovery rates. These changes in turn influence the ease of plastic deformation (and frictional work) until a dynamic balance is achieved. At this stage the average local temperatures of the friction couple remain constant and recovery just compensates for the additional work hardening caused by plastic deformation during sliding. Also, at each local asperity contact, the surface stress and stain increase from some initial value (which depends on stress-strain history) to some final value. Relaxation or recovery can occur almost simultanously or during the intervals between asperity contacts. In the quasi-steady-state contact the final stress equals the initial stress value, ensuring that contact state repeats itself. Thus, despite the fact that the

plastic deformation and wear continuously change the surface topography on a local scale, the global roughness, conditions of debris entrapment and physical properties of the materials remain statistically invariant and characterize the contact state. It follows that each frictional component maintains a fixed proportional contribution to the total and that each can be analysed with the results superposed to yield the overall friction for a given tribosystem."

The derivation of this model is long, so here the assumptions and results are described, and the derivation is merely outlined.

Consider two materials in contact, where material-1 is harder than material-2. Usually material-1 is the tool and material-2 is the workpiece. The total plastic deformation energy is

$$E_{dj} = \sum_{i=1}^{N_j} A_{ij}\, \delta x\, \tau_j' f\left(\frac{\tau_{ij}}{\tau_j'}\right) \qquad j = 1,2 \tag{2.21}$$

where: A_{ij} is the individual contact area,
N_j is the number of individual contacts,
δx is the virtual sliding distance,
τ_j' is the ultimate shear strength of material j,
τ_{ij} is the shear stress of contact i within material j, and

$$f(\zeta) = 1 + \frac{\zeta - 2\ln(1+\zeta)}{\ln(1-\zeta^2)}.$$

Equate the frictional work done to the plastic deformation energy stored in both materials and solve for the coefficient of friction during sliding μ_s:

$$\mu_s = \underbrace{\sum_{i=1}^{N_1} \left(\frac{A_{i1}}{P}\right) \tau_i' f\left(\frac{\tau_{i1}}{\tau_1'}\right)}_{\text{material 1}} + \underbrace{\sum_{i=1}^{N_2} \left(\frac{A_{i2}}{P}\right) \tau_i' f\left(\frac{\tau_{i2}}{\tau_2'}\right)}_{\text{material 2}}. \tag{2.22}$$

where: A_{i1}, A_{i2} are the areas of individual contacts, and
P is the normal force.

This equation suggests that in order to find μ one has to find the individual contributions of each contact interaction. Confining our contact types to asperity adhesion, asperity ploughing (from interlocking asperities) and debris ploughing, we thus have the total area of contact A as

$$A = A_{aa} + A_{ap} + A_d = (1 - \chi)A_a + \chi A_a + A_d \tag{2.23}$$

where: A_{aa} is the average area of asperity adhesion,
A_{ap} is the average area of asperity ploughing, and
A_d is the average area of debris ploughing;
A_a is the average area of asperity contact, and
χ is the proportion of asperity contacts that are ploughing.

Similarly, the normal force P can be apportioned between the individual loads

$$P = (1 - \chi)P_a + \chi P_a + P_d. \tag{2.24}$$

Where: P_a is the load on the asperities, and
P_d is the load on the debris particles.

So it is necessary only to consider the average contributions of each contact phenomenon.

A simple geometry was chosen for the model of the real asperities. The shape of each asperity is conical with a hemispherical tip of constant radius. The asperities are assumed to have a normal (Gaussian) distribution of heights. The debris particles are modelled by spheres for simplicity. Debris particles usually have much greater hardness than the parent materials, and so are assumed to be rigid. From these assumptions the stresses for asperity adhesion, ploughing and debris ploughing can be found. These stresses for the simplified geometry are averaged over the contact area assuming a homogeneous and isotropic distribution of asperities and debris.

The final result is

$$\mu_s = \frac{S_1}{P}\left[(1-\chi)A_a f\left(\frac{\tau_{a1}}{S_1}\right) + \chi A_a + A_{d1}\right] + \frac{S_2}{P}\left[(1-\chi)A_a f\left(\frac{\tau_{a2}}{S_2}\right) + \chi f\left(\frac{S_1 H_1}{S_2 H_2}\right) + A_{d2}\right]. \quad (2.25)$$

where: S_1, S_2 are the shear stress strengths,
H_1, H_2 are the hardnesses, and
τ_{a1}, τ_{a2} are the adhesive stresses in each material.

This is now used for the coefficient of friction for sliding with either the Amontons-Coulomb or WVS model for the nonsliding sticking state. The algorithm presented for AC is modified to use equation (2.25) for the slipping state, and a constant μ otherwise.

2.4 Wilson Model of Lubrication

So far all three friction models described have been dry models where there is no lubricant between surfaces. Now in practice this is not the common situation as most metal forming processes use lubricated work pieces. In order to model friction with lubrication, the lubricant must be described also. No longer is it merely metal on metal contact as the lubricant will separate the surfaces, except in the case when the film is thinner than the height of the asperities. The various types of contact with lubricant will be described below.

Wilson, et al. [35] have proposed a friction model incorporating a film of lubricant covering the work piece. The pressure distribution and the film thickness in the lubricant are described by the rough Reynolds equation proposed by Patir & Cheng [19], which takes into account the roughness of the tool and workpiece surfaces. The frictional stresses are given by different models depending on the state of the lubricant.

The following assumptions are made for the lubricant:

1. Body forces are neglected (no dynamical effects in lubricant).

2. The pressure is constant through the thickness of the film.
3. The surfaces of the two contacting bodies are flat locally; velocities are parallel to the surfaces.
4. There is no slip at the surfaces, so that the layer of lubricant next to a surface has the same velocity as the surface.
5. The lubricant is Newtonian.
6. The flow is laminar.
7. Fluid inertia is neglected.
8. The viscosity is constant.

This results in the Reynolds equation which describes the pressure and film thickness (see e.g. [7]) for the case of smooth surfaces:

$$\frac{\partial}{\partial x}\left(\frac{h^3}{12\eta}\frac{\partial p}{\partial x}\right)+\frac{\partial}{\partial y}\left(\frac{h^3}{12\eta}\frac{\partial p}{\partial y}\right) = \frac{\partial}{\partial x}\left(\frac{V_1+V_2}{2}\right)h+\frac{\partial}{\partial y}\left(\frac{W_1+W_2}{2}\right)h+\frac{\partial h}{\partial t} \quad (2.26)$$

where: p is the pressure,
h is the film thickness,
η is the lubricant viscosity,
V_1, V_2 are the x-velocities and
W_1, W_2 are the y-velocities for the tool and work surfaces respectively.

Patir & Cheng [19] considered the case of two parallel rollers in contact. Then $W_1 = W_2 = 0$ and the second term in the rhs of equation (2.26) vanishes. To take into account the effect of asperities on the lubricant behaviour, the flow of lubricant over a small volume containing few asperities is considered. The result is then averaged over the larger surface to obtain the average thickness and pressure of the lubricant. Roughness of a surface i refers to the standard deviation σ_i of the mean surface amplitude δ_i so that the combined surface amplitude $\delta = \delta_1+\delta_2$ has roughness $\sigma = \sqrt{\sigma_1^2+\sigma_2^2}$, i.e. the combined standard

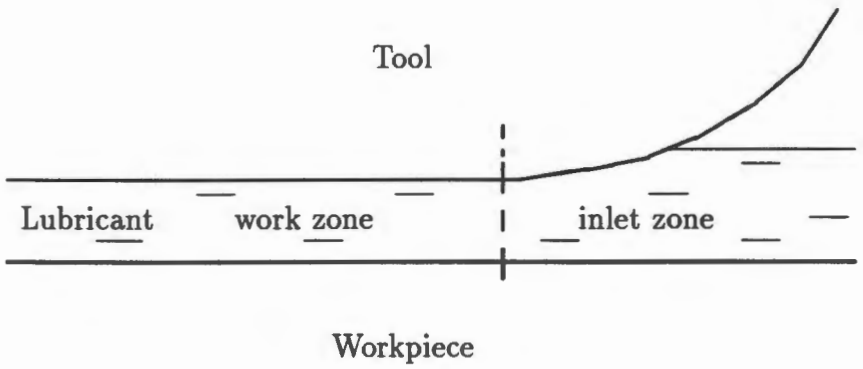

Figure 2.4: The inlet and work zones.

deviation. Using this method, Patir & Cheng derived the average Reynolds equation[1], giving the average pressure and thickness:

$$\frac{\partial}{\partial x}\left(\phi_x \frac{\bar{h}^3}{12\eta}\frac{\partial \bar{p}}{\partial x}\right) + \frac{\partial}{\partial y}\left(\phi_y \frac{\bar{h}^3}{12\eta}\frac{\partial \bar{p}}{\partial y}\right) = \frac{V_1 + V_2}{2}\frac{\partial \bar{h}}{\partial x} + \frac{V_1 - V_2}{2}\sigma\frac{\partial \phi_s}{\partial x} + \frac{\partial \bar{h}}{\partial t} \qquad (2.27)$$

where: $\bar{p}$ is the average pressure,
$\bar{h}$ is the average film thickness,
ϕ_x, ϕ_y are the pressure flow factors,
σ is the composite surface roughness, and
ϕ_s is the shear flow factor.

The contact surface is divided into two regions: the inlet zone and the work zone. This is illustrated in figure 2.4. The boundary conditions for equations (2.26) and (2.27) will be different in the two zones.

In order to solve these equations easily the plane strain and axisymmetric cases are used.

[1]This is also known as the rough Reynolds equation.

2.4.1 Plane Strain Case

The plane strain case is appropriate for those problems which are already by nature plane strain, or where the velocities of the surfaces are always parallel. In computational work where the bodies can be approximated by plane strain the contact surface is one-dimensional and the lubricant would naturally be approximated as plane strain. The example used below is two dimensional plane strain rolling of a strip.

Inlet zone

For the inlet zone, under conditions of isothermal plane strain and thick film, the smooth Reynolds equation is

$$\frac{\partial}{\partial x}\left(\frac{h^3}{12\eta}\frac{\partial p}{\partial x}\right) = \frac{\partial}{\partial x}\left(\bar{V}h\right) + \frac{\partial h}{\partial t} \tag{2.28}$$

where $\bar{V} = \frac{1}{2}(V_1 + V_2)$ is the average surface speed.

And the rough Reynolds equation for the same conditions is

$$\frac{\partial}{\partial x}\left(\phi_x\frac{\bar{h}^3}{12\eta}\frac{\partial \bar{p}}{\partial x}\right) = \frac{V_1 + V_2}{2}\frac{\partial \bar{h}}{\partial x} + \frac{V_1 - V_2}{2}\sigma\frac{\partial \phi_s}{\partial x} + \frac{\partial \bar{h}}{\partial t}. \tag{2.29}$$

For isotropic surface roughness the flow factors have the simple expressions given by Tripp [32]

$$\phi_x = 1 - \frac{3}{2}\left(\frac{\sigma}{\bar{h}}\right)^2, \tag{2.30}$$

$$\phi_s = \frac{3}{2}\frac{\sigma}{\bar{h}}\left(\frac{\sigma_1^2 - \sigma_2^2}{\sigma^2}\right), \tag{2.31}$$

where: σ_1, σ_2 are the surface roughnesses, and
σ is the combined surface roughness.

These arise from considering isotropic asperities with a normal distribution of heights.

Work zone

In the work zone it is assumed that the pressure gradient term has a negligable influence on lubricant flow (see Wilson & Wang [37]). In the work zone it is possible to choose coordinates such that $V_1 = V$ and $V_2 = 0$. Equation (2.28) without the pressure gradient term is thus

$$\frac{\partial}{\partial x}\left(\tfrac{1}{2}Vh\right) + \frac{\partial h}{\partial t} = 0, \tag{2.32}$$

which can be decomposed into two ordinary differential equations

$$\frac{dx}{dt} = \tfrac{1}{2}V, \tag{2.33}$$

$$\frac{dh}{dt} = -\tfrac{1}{2}\frac{\partial}{\partial x}(Vh). \tag{2.34}$$

In the rough case the surface velocities vary with position in the work zone and equation (2.29) must be extended to

$$\frac{\partial}{\partial x}\left(\phi_x \frac{\bar{h}^3}{12\eta}\frac{\partial \bar{p}}{\partial x}\right) = \frac{\partial}{\partial x}\left(\frac{V_1 + V_2}{2}\bar{h} + \frac{V_1 - V_2}{2}\sigma\phi_s\right) + \frac{\partial \bar{h}}{\partial t}. \tag{2.35}$$

In the rough work zone choose coordinates such that $V_1 = V$ and $V_2 = 0$, and drop the pressure gradient term to obtain

$$\frac{\partial}{\partial x}\left(\tfrac{1}{2}V\bar{h} + \tfrac{1}{2}V\sigma\phi_s\right) + \frac{\partial \bar{h}}{\partial t} = 0, \tag{2.36}$$

which can be decomposed into two ordinary differential equations:

$$\frac{dx}{dt} = \tfrac{1}{2}V\left(1 - \frac{\sigma}{\bar{h}}\right), \tag{2.37}$$

$$\frac{d\bar{h}}{dt} = -\tfrac{1}{2}\frac{\partial}{\partial x}\left[V\left(1 - \frac{\sigma}{\bar{h}}\right)\right]. \tag{2.38}$$

2.4.2 Axisymmetric Case

The axisymmetric case is appropriate wherever the geometry exhibits cylindrical symmetry. The examples used below are hemispherical punching, and axisymmetric cup deep-drawing. In [36] the example of axisymmetrical stretch-forming is used.

In the axisymmetric case the Reynolds equation must be modified to take into account local flow geometry. The isothermal, smooth equation for the inlet zone is then

$$\frac{\partial}{\partial s}\left(\frac{rh^3}{12\eta}\frac{\partial p}{\partial s}\right) = \frac{\partial}{\partial s}\left(r\bar{V}h\right) + r\frac{\partial h}{\partial t} \tag{2.39}$$

where: s is the lubricant stream length, and
r is the radial coordinate.

The lubricant stream length s is measured from the axis of symmetry *along* the work piece.

For the work zone, dropping the pressure gradient term as before, and choosing coordinates so that $V_1 = V$ and $V_2 = 0$ gives

$$\frac{\partial}{\partial s}\left(\tfrac{1}{2}Vrh\right) + r\frac{\partial h}{\partial t} = 0. \tag{2.40}$$

This is decomposable into two ODEs as before

$$\frac{ds}{dt} = \tfrac{1}{2}V, \tag{2.41}$$

$$\frac{dh}{dt} = \frac{hV}{2r}\frac{\partial r}{\partial s} - \tfrac{1}{2}rh\frac{\partial V}{\partial s}. \tag{2.42}$$

The rough surfaces equation, with flow factors ϕ_s and ϕ_r, for the inlet zone is

$$\frac{\partial}{\partial s}\left(\phi_x\frac{r\bar{h}^3}{12\eta}\frac{\partial \bar{p}}{\partial s}\right) = \frac{V_1+V_2}{2}\frac{\partial}{\partial s}r\bar{h} + \frac{V_1-V_2}{2}\sigma\frac{\partial}{\partial s}r\phi_s + r\frac{\partial \bar{h}}{\partial t}. \tag{2.43}$$

And for the work zone, dropping the pressure gradient term as before, with $V_1 = V$ and $V_2 = 0$ gives

$$\frac{\partial}{\partial s}\left(\tfrac{1}{2}Vr\bar{h} + \tfrac{1}{2}Vr\sigma\phi_s\right) + r\frac{\partial \bar{h}}{\partial t} = 0, \tag{2.44}$$

This is decomposable into two ODEs as before

$$\frac{ds}{dt} = \tfrac{1}{2}V\left(1 - \frac{\sigma}{\bar{h}}\phi_s\right), \tag{2.45}$$

$$\frac{d\bar{h}}{dt} = \frac{hV}{2r}\left(1 - \frac{\sigma}{\bar{h}}\phi_s\right)\frac{\partial r}{\partial s} - \tfrac{1}{2}r\bar{h}\frac{\partial V}{\partial s}. \tag{2.46}$$

2.4.3 Frictional stress

Once the average pressure and thickness of the film are known, the type of friction can be determined and the appropriate friction model used to calculate the frictional stresses.

The thick film regime occurs when $h > 10\sigma$. Then the friction is due entirely to viscous shear τ_h which is given by

$$\tau_h = \frac{\eta(V_1 - V_2)}{h}, \tag{2.47}$$

where η is the lubricant dynamic viscosity.

The thin film regime occurs for $3\sigma < h \leq 10\sigma$. Friction is still due to viscous shear, but is affected by roughness:

$$\tau_{h1} = \phi_{f1}\frac{\eta(V_1 - V_2)}{h}, \tag{2.48}$$

where ϕ_{f1} is the shear stress factor which takes care of the effects of roughness. We use the expression calculated by Pater & Cheng [20]

$$\phi_{f1} = \frac{35}{32}\left[(1 - z^3)^2 \ln\left(\frac{z+1}{z-1}\right) + \frac{z}{15}\{66 + z^2(30z^2 - 80)\}\right] \tag{2.49}$$

where $z = h/3\sigma$.

When $h \leq 3\sigma$ the interface is in the mixed or boundary regimes. To determine which, the mean lubricant pressure in the valleys p_b is calculated, assuming the mixed regime. If $p_b > 0$ then it is indeed in the mixed regime otherwise it is in the boundary regime.

Wilson's mixed model [34] gives the mean lubricant pressure in the valleys as

$$p_b = p - AHS \tag{2.50}$$

where: p is the pressure in the main part of the lubricant film,
A is the fractional contact area,
H is the effective hardness, and
S is the sheet shear strength.

From Christensen [8] we approximate the fractional contact area A as

$$A = \tfrac{35}{32}\left[\tfrac{16}{35} - z + z^3 - \tfrac{3}{5}z^5 + \tfrac{1}{7}z^7\right], \qquad z = h/3\sigma. \tag{2.51}$$

From Wilson & Shea [36] the effective hardness is given by

$$H = \frac{2}{f_1(A)E + f_2(A)}$$

where

$$\begin{aligned} E &= \frac{l\dot{\epsilon}}{\theta_t(V_1 - V_2)} \\ f_1(A) &= 0.515 + 0.345 - 0.86A^2 \\ f_2(A) &= \left(2.571 - A - A\ln(1-A)\right)^{-1} \end{aligned}$$

where: l is the asperity half spacing,
$\dot{\epsilon}$ is the strain rate, and
θ_t is the mean slope of tool asperities.

Mixed lubrication occurs when the mean lubricant pressure in the valleys p_b is positive. Then the friction stress τ_m, which consists of asperity ploughing τ_p and adhesion τ_a stresses as well as lubricant shearing τ_{h2}, is given by

$$\tau_m = \tau_a A + \tau_p A + \tau_{h2}(1 - A) \tag{2.52}$$

where

$$\tau_a = kS \tag{2.53}$$

$$\tau_p = \theta_t H S \tag{2.54}$$

$$\tau_{h2} = \phi_{f2} \frac{\eta(V_1 - V_2)}{h} \tag{2.55}$$

where k is an adhesion coefficient, and from [20]

$$\phi_{f2} = \tfrac{35}{32} z \Big[(1 - z^2)^3 \ln 300(z + 1) + \tfrac{1}{60} \{ -55 + z[132 + z(345 + z(-160 + z(-405 + z(60 + 147))))] \} \Big],$$

where $z = h/3\sigma$.

Boundary lubrication occurs when the mean lubricant pressure in the valleys p_b is negative, and only the adhesion and ploughing stresses are present. These are calculated as before in equations (2.53)–(2.55). The fractional contact area A is calculated from equation (2.50) assuming that the mean lubricant pressure in the valleys p_b is zero [33]. And then the boundary regime frictional stress is given by

$$\tau_b = (\tau_a + \tau_p)A. \tag{2.56}$$

Algorithm for calculating the Wilson model stresses

In the processes modelled herein the inlet zone is characterized by a circular surface meeting a flat surface as in figure 2.5. The inlet zones for the three processes are shown in figures 2.6–2.8. So, for the inlet zone the thickness of the lubricant will be determined by the curvature of the roller or punch/die edge.

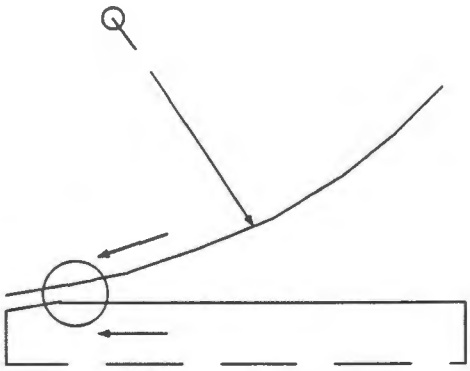

Figure 2.5: The inlet zone for rolling.

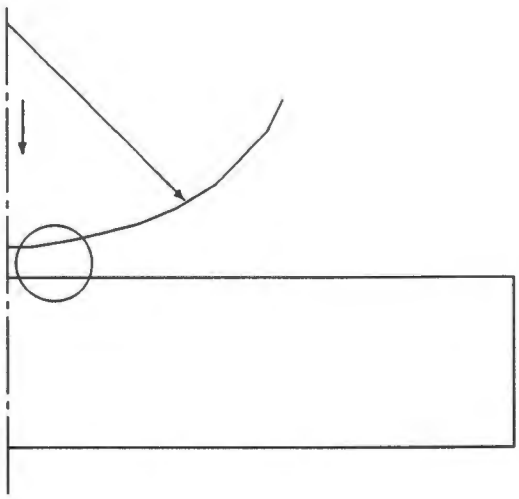

Figure 2.6: The inlet zone for punching.

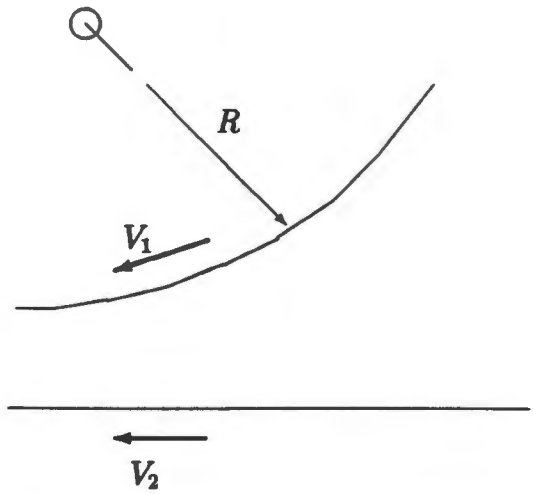

Figure 2.7: The geometry of the inlet zone.

We use the parabolic approximation for the circular arc, then the thickness of the lubricant at time t and position x is given by

$$h(t,x) = h_0(t) + \frac{x^2}{2R} \tag{2.57}$$

where: $h_0(t)$ is the thickness of film at $x = 0$ for any time t, and
R is the radius of the arc.

This simplifies the integration of the equations. The boundary conditions for the inlet zone are, at time t, for the left boundary,

$$x = 0: \quad h = h_0(t) \quad p = p_0(t) \quad \frac{\partial p}{\partial x} = 0, \tag{2.58}$$

and for the right boundary,

$$x = \infty: \quad h = \infty \quad p = 0, \tag{2.59}$$

where $p_0(t)$ is the pressure at $x = 0$ for time t.

Contact boundary conditions, for pressure and lubricant thickness, in the work zone are given by the solution of equation (2.28) for the smooth plane strain and equation (2.29) for the rough plane strain cases; and by equations (2.39)

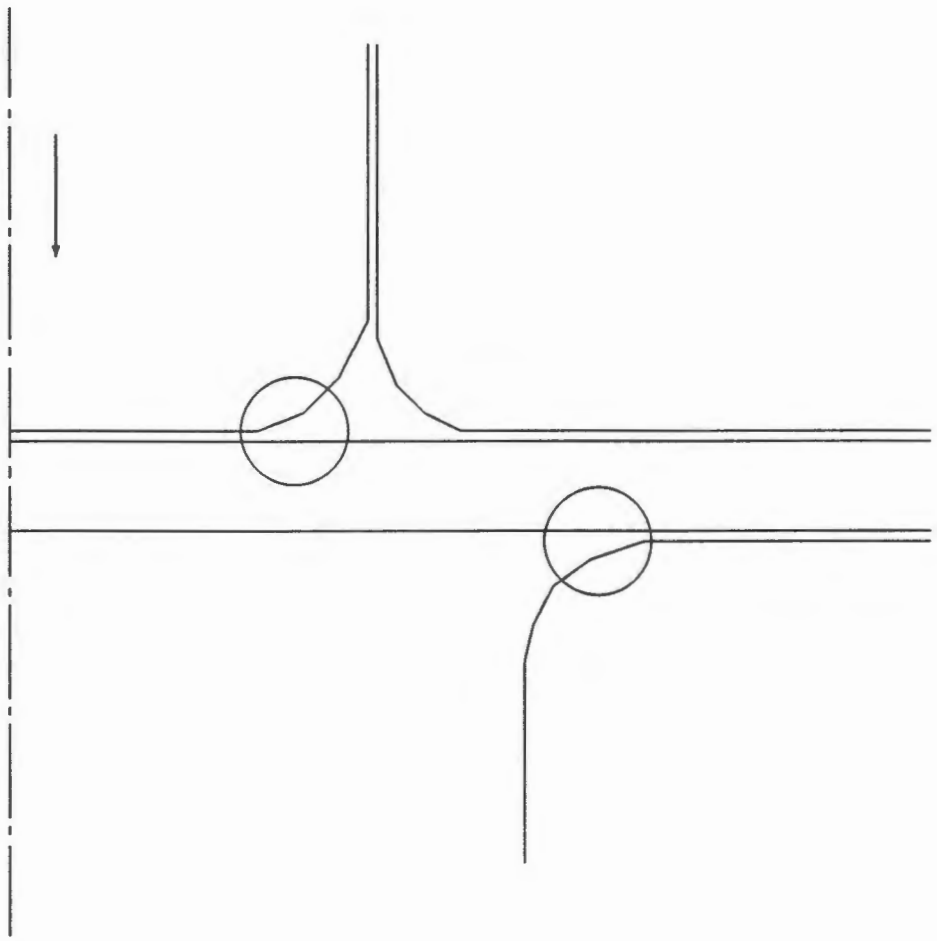

Figure 2.8: The inlet zones for deep drawing.

for the smooth axisymmetric and equation (2.43) for the rough axisymmetric cases. Once the thickness and pressure are known the frictional stress is calculated by the appropriate equations for the current lubrication regime.

In order to numerically integrate the ODEs, obtained from the PDE, for the work zone it is necessary to approximate the $\partial/\partial x$ term in equations (2.34) and (2.38), and the $\partial/\partial s$ term in equations (2.42) and (2.46). This is done by using linear interpolation over adjacent calculation points.

Chapter 3

Formulation of Nonstationary Contact Problem

3.1 Introduction

3.1.1 Processes simulated

The following four metalforming processes are simulated within the finite element method:

- 3-dimensional rolling of a metal strip,
- 2-dimensional plane strain rolling of a strip,
- hemispherical punching of a disc, and
- axisymmetric cup deep-drawing.

3.1.2 Notation

In this chapter indexed tensor notation will be used. The indices I to L will refer to the general coordinates in the total Lagrangian frame, indices i to l will refer to the updated Lagrangian reference frame. On a surface, stresses and displacements will be split into a normal part, indicated by the subscript N, and a tangental part, indicated by the subscript T, where T runs over the two tangental directions.

When necessary, vectors will be shown as bold figures without the tensor index and tensors of higher order will be shown as bold italic figures without indices. Time will be indicated by t. The following special spaces and tensors will be used:

$\mathcal{C}^2$ is the vector space of real functions that are continuously differentiable to second order,
$\mathcal{H}^2$ is a Sobolev space of $\mathcal{L}_2$ elements with first order generalised derivatives in $\mathcal{L}_2$, and
$\mathcal{L}_2$ is the space of square integrable functions, i.e., $\int_\Omega |u(x)|^2\,dx < \infty$ for $u \in \mathcal{L}_2$;
S_{KL} is the second Piola-Kirchhoff stress tensor,
$u_{L,K}$ is the displacement gradient,
ρ_0 is the initial density,
L^{EP}_{IJKL} is the elastic-plastic hyperoperator,
$\dot{\varepsilon}_{KL}$ is the Green-Lagrange strain rate, and
$\dot{S}_{IJ}$ is the stress rate.

3.2 Total Lagrangian Formulation

The derivation here follows the paper [25]. The body at time t is ${}^t\Omega$ with surface $\partial {}^t\Omega = {}^t\Gamma$. The surface is separated into the contact surface ${}^t\Gamma_S$, the surface subject to displacement boundary conditions ${}^t\Gamma_U$, and the surface subject to stresses and forces ${}^t\Gamma_F$, and the surface free of constraints, ${}^t\Gamma_{\mathrm{free}}$:

$$ {}^t\Gamma = {}^t\Gamma_U \cup {}^t\Gamma_F \cup {}^t\Gamma_S \cup {}^t\Gamma_{\mathrm{free}}. $$

3.2.1 Elastic-plastic body motion

The motion of an elastic-plastic body is governed by the equation of motion (the differential form of the balanced generalised forces) and the elastic-plastic constitutive relation. The equation of motion with body forces $\rho_0 t_I$ and inertia forces $\rho_0 f_I$ is

$$(S_{KL}\delta_{LI} + S_{KL}u_{L,I})_{,K} + \rho_0 f_I = \rho_0 t_I, \tag{3.1}$$

in ${}^t\Omega \times (t_i, t_i + \Delta t)$, for $u_I \in C^2$.

The material is elastic-plastic with constitutive relation

$$\dot{S}_{IJ} = L^{\mathrm{EP}}_{IJKL}\dot{\varepsilon}_{KL} \tag{3.2}$$

in ${}^t\Omega \times (t_i, t_i + \Delta t)$.

3.2.2 Boundary conditions

The ordinary boundary conditions are specified by displacements, stresses, forces and stress vectors. For displacements we have

$$u_I = \phi_I(\mathbf{x}, \xi)$$

on ${}^t\Gamma_U \times (t_i, t_i + \Delta t)$. At least at one point $\mathcal{P}$ it is necessary to assume von Neumann homogeneous conditions

$$\phi_I(\mathbf{x}, \xi) = 0 \qquad \text{and} \qquad \frac{\partial \phi_I}{\partial \mathbf{N}} = 0$$

at $\mathcal{P} \in {}^t\Gamma_U \times (t_i, t_i + \Delta t)$, which is needed to ensure the existance and uniqueness of a solution, as proved by Ronda [25]. This point $\mathcal{P}$ varies across the processes simulated. For punching it is the node at the centre of the bottom of the disc. For rolling it is the node suspended by the spring, which is theoretically rigid,

but in practice it is flexible. For deep drawing the point $\mathcal{P}$ is the centre of the upper layer of the blank directly under the punch, which is sticking to the punch and moves downwards with it.

For stresses and forces use

$$(S_{KL}\delta_{LI} + S_{KL}u_{L,I})N_K = F_I$$

on the surface subject to streses and forces ${}^t\Gamma_F \times (t_i, t_i + \Delta t)$.

On the contact surface define a general friction boundary condition which gives the frictional force as a function of other variables, such as pressure, displacement, film thickness, roughness, etc.

$$F_T = \mathcal{F}_T(\ldots)$$

on ${}^t\Gamma_S \times (t_i, t_i + \Delta t)$.

The initial conditions for the body motion are

$$u_I(\mathbf{x}, 0) = 0 \qquad \text{and} \quad \dot{u}_I(\mathbf{x}, 0) = 0$$

on ${}^t\Omega \times (t_i, t_i + \Delta t)$.

3.2.3 Frictional boundary conditions

The explicit forms for the function $\mathcal{F}$, which defines the tangental contact forces, for the four friction models described in chapter 2 are given below.

AC model

Define $f = \|\mathbf{t}\| - \mu p$ then

$$\mathcal{F} = \begin{cases} -g\mathbf{u} & \text{if } f \leq 0 \\ -\mu p \operatorname{sgn} \mathbf{u} & \text{if } f > 0 \end{cases} \tag{3.3}$$

WVS model

Define $f = \|\mathbf{t}\| - \alpha p^{\nu} - \beta p$ then

$$\mathcal{F} = \begin{cases} -g\mathbf{u} & \text{if } f \leq 0 \\ -(\alpha p^{\nu} + \beta p)\,\operatorname{sgn}\mathbf{u} & \text{if } f > 0 \end{cases} \tag{3.4}$$

QSS model

Define $f = \|\mathbf{t}\| - \mu p$ then

$$\mathcal{F} = \begin{cases} -g\mathbf{u} & \text{if } f \leq 0 \\ -\mu_s p\,\operatorname{sgn}\mathbf{u} & \text{if } f > 0 \end{cases} \tag{3.5}$$

where μ_s is the coefficient of friction for sliding given in section 2.4.

Wilson model

Rather than a simple yield function this model depends on the thickness of lubricant h which is subject to the Reynolds partial differential equation. Once h is known the expression for friction is:

$$\mathcal{F} = \begin{cases} \tau_h & \text{if } h \geq 10\sigma \\ \tau_{h1} & \text{if } 10\sigma > h \geq 3\sigma \\ \tau_m & \text{if } h < 3\sigma \text{ and } p_b > 0 \\ \tau_b & \text{if } h < 3\sigma \text{ and } p_b < 0 \end{cases} \tag{3.6}$$

where the expressions for the various τ are given in section 2.5.

3.2.4 Weak form of equation of motion

The weak form of the equation of motion is obtained by taking the scalar product of the differential operator, defined by equation (3.1),

$$\mathcal{D}(S_{IJ}, u_K) = (S_{KL}\delta_{LI} + S_{KL}u_{L,I})_{,K} + \rho_0 f_I - \rho_0 t_I$$

and $(\mathbf{v} - \dot{\mathbf{u}})$, where $\mathbf{v} \in \mathcal{H}^2$ is a test function and $\dot{\mathbf{u}}$ is the unknown rate of displacement. Using Green's integeral theorem suitable for the space $\mathcal{H}^2$ then gives

$$\begin{aligned}
&\int_{{}^t\Omega} (S_{KL}\delta_{LI} + S_{KL}u_{L,I})(v_{I,K} - \dot{u}_{I,K})\, dV - \int_{{}^t\Gamma_F} F_I(v_I - \dot{u}_I)\, d\gamma \\
&- \int_{{}^t\Gamma_U} F_I(v_I - \dot{u}_I)\, d\gamma - \int_{{}^t\Gamma_S} \{F_N(v_N - \dot{u}_N) + \mathcal{F}_T(v_T - \dot{u}_T)\}\, d\gamma \\
&+ \int_{{}^t\Omega} \rho_0 f_I(v_I - \dot{u}_I)\, dV + \int_{{}^t\Omega} \rho_0 t_I(v_I - \dot{u}_I) = 0, \qquad (3.7)
\end{aligned}$$

where $u_I, v_I \in \mathcal{H}^2$.

3.2.5 Incremental relations

Functional (3.7) contains unknown stresses, forces and displacements. Stresses and forces can be eliminated by the use of the constitutive relations, but this needs a formulation in terms of increments of the constitutive variables, because the constitutive equations are of the rate type. For the finite deformation of an elastic-plastic material the incremental relations (see [2]) are given below.

The increment in stress over the interval $[t, t + \Delta t]$ is

$${}_0^{t+\Delta t}S_{IJ}(\xi) = {}_0^tS_{IJ} + {}_0S_{IJ}(\xi). \qquad (3.8)$$

where:

${}^{t}_{0}S_{IJ}$ is the initial stress measured at the beginning of the time step referred to the initial configuration at time 0;

${}_{0}S_{IJ}(\xi)$ is the increment in stress appearing during this time step,

${}^{t+\Delta t}_{0}S_{IJ}(\xi)$ is the stress at time ξ referred to the initial configuration, and which depends on $\xi \in [t, t+\Delta t]$.

The superscript on the left of a variable refers to the time at which that variable is measured, and the subscript appearing on the left of a variable refers to the time with which the measurement is referred. The increment appearing in (3.8) is a function of $\xi \in [t, t+\Delta t]$.

The strain at time $t+\Delta t$ is

$$ {}^{t+\Delta t}_{0}\varepsilon_{IJ} = {}^{t}_{0}\varepsilon_{IJ} + {}_{0}\varepsilon_{IJ} $$

where ${}_{0}\varepsilon_{IJ}$ is the strain increment, which is seperable into linear and nonlinear parts

$$ {}_{0}\varepsilon_{IJ} = {}_{0}e_{IJ} + {}_{0}\eta_{IJ} \tag{3.9} $$

where the linear part is given by

$$ {}_{0}e_{IJ} = \frac{1}{2}\left({}_{0}u_{I,J} + {}_{0}u_{J,I} + {}^{t}_{0}u_{I,K}\,{}_{0}u_{K,J} + {}_{0}u_{I,K}\,{}^{t}_{0}u_{K,J}\right), $$

where ${}^{t}_{0}u_{I,K}$ and ${}^{t}_{0}u_{K,J}$ are known from the resultant displacement at the end of the previous time step, and a nonlinear part, which is defined by

$$ {}_{0}\eta_{IJ} = \tfrac{1}{2}\,{}_{0}u_{I,K}\,{}_{0}u_{K,J}. $$

According to the flow rule, the plastic strain increment is defined by

$$ {}_{0}\varepsilon^{\mathrm{P}}_{KL} = {}^{t}\Lambda \frac{\partial {}^{t}Y}{\partial {}^{t}_{0}S_{KL}} \tag{3.10} $$

where an inelastic factor is given by

$$ {}^t\Lambda = \frac{{}^t\boldsymbol{q}^{\mathrm{T}}\, \boldsymbol{L}^{\mathrm{E}}\, {}_0\boldsymbol{\varepsilon}}{{}^t\boldsymbol{p}^{\mathrm{T}}\, {}^t\boldsymbol{q} + {}^t\boldsymbol{q}^{\mathrm{T}}\, \boldsymbol{L}^{\mathrm{E}}\, {}^t\boldsymbol{q}}, $$

$$ {}^tq_{IJ} = \frac{\partial {}^tY}{\partial {}^tS_{IJ}} \qquad \text{and} \qquad {}^tp_{IJ} = \frac{\partial {}^tY}{\partial {}^t\varepsilon^{\mathrm{P}}_{IJ}}, $$

and the yield condition is

$$ {}^tY\left({}^t_0S_{IJ}, {}^t\kappa\right) = 0 $$

with a work hardening parameter ${}^t\kappa$. The constitutive equation for the elastic increment is

$$ {}_0S_{IJ} = L^{\mathrm{E}}_{IJKL}\, {}_0\varepsilon^{\mathrm{E}}_{KL}. \tag{3.11} $$

The total strain rate is decomposed into an elastic strain rate and a plastic strain rate

$$ {}_0\dot{\varepsilon}_{IJ} = {}_0\dot{\varepsilon}^{\mathrm{E}}_{IJ} + {}_0\dot{\varepsilon}^{\mathrm{EP}}_{IJ}. \tag{3.12} $$

For an increment Δt, this yields the decomposition of the total strain increment:

$$ {}_0\varepsilon_{IJ} = {}_0\varepsilon^{\mathrm{E}}_{IJ} + {}_0\varepsilon^{\mathrm{EP}}_{IJ}. \tag{3.13} $$

Using equations (3.9)–(3.13) gives the constitutive equation for an elastic-plastic material:

$$ {}_0\boldsymbol{S} = {}^t\boldsymbol{L}^{\mathrm{EP}}\, {}_0\boldsymbol{\varepsilon} $$

where the elastic-plastic hyperoperator is defined by

$$ {}^t\boldsymbol{L}^{\mathrm{EP}} = \boldsymbol{L}^{\mathrm{E}} - \frac{\boldsymbol{L}^{\mathrm{E}}\, {}^t\boldsymbol{q} ({}^t\boldsymbol{q})^{\mathrm{T}}}{{}^t\boldsymbol{p}^{\mathrm{T}}\, {}^t\boldsymbol{q} + {}^t\boldsymbol{q}^{\mathrm{T}}\, \boldsymbol{L}^{\mathrm{E}}\, {}^t\boldsymbol{q}}. $$

3.3 Updated Lagrangian Formulation

In the updated (modified) Lagrangian formulation particle motion is described by a sequence of reference configurations where the time range is divided into time intervals $[t_i; t_i + \Delta t]$. We use the stress incremental relation

$$ {}_t^{t+\Delta t}S_{ij}(\xi) = {}^t\tau_{ij} + {}^tS_{ij}(\xi), \qquad {}_t^tS_{ij}(0) = {}^t\tau_{ij}, \tag{3.14} $$

where we use the notation ${}_t^{t+\Delta t}S_{ij}$ to denote the second Piola- Kirchhoff stress defined at time $t + \Delta t$ with reference to the configuration at time t, and ${}^tS_{ij}$ is the stress increment appearing during time period Δt. We further simplify the notation as follows:

$$ {}^{n+1}S_{ij} = {}_n^{n+1}S_{ij} = {}_t^{t+\Delta t}S_{ij}, \qquad {}^n\tau_{ij} = {}^t\tau_{ij}, \qquad {}^nS_{ij} = {}^tS_{ij}, $$

where n is the number of the time step.

3.3.1 Incremental equations

The incremental relations for the updated Lagrangian are given here.

The equation of motion for the time step $n + 1$ becomes, with body forces ${}^{n+1}\rho\,{}^{n+1}t_i$ and inertia forces ${}^{n+1}\rho\,{}^{n+1}f_i$,

$$ ({}^{n+1}S_{kl}\delta_{il} + {}^{n+1}S_{kl}u_{i,l})_{,k} + {}^{n+1}\rho\,{}^{n+1}f_i = {}^{n+1}\rho\,{}^{n+1}t_i. $$

The stress incremental relation is

$$ {}^{n+1}S_{ij}(\xi) = {}^n\tau_{ij} + {}^nS_{ij}(\xi), \qquad {}^{n+1}S_{ij}(0) = {}^n\tau_{ij} $$

where $\xi \in (0, \Delta t)$, and the initial stress calculation for the $n + 1$ step is

$$ {}^{n+1}\tau_{ij} = \frac{{}^{n+1}\rho}{{}^n\rho}\,{}_n^{n+1}x_{i,m}\,{}^{n+1}S_{mp}\,{}_n^{n+1}x_{pj}, $$

where ${}^{n+1}_{n}x_{ij}$ is the gradient tensor at step $n+1$ with reference to step n. The total Green-Lagrange strain, equivalent now to the increment of strain, generated at Δt is separated into a sum of linear and nonlinear parts:

$$ {}^{n}\varepsilon_{ij} = {}^{n+1}_{n}\varepsilon_{ij} = {}^{n}e_{ij} + {}^{n}\eta_{ij} $$

$$ {}^{n}e_{ij} = \tfrac{1}{2}({}^{n}u_{i,j} + {}^{n}u_{j,i}) \qquad {}^{n}\eta_{ij} = \tfrac{1}{2}\,{}^{n}u_{k,i}\,{}^{n}u_{k,j}. $$

The elastic-plastic material constitutive equation is

$$ {}^{n}S_{ij} = {}^{n}C^{\mathrm{EP}}_{ijkl}\,{}^{n}\varepsilon_{kl}. $$

The boundary conditions in terms of displacement are

$$ {}^{n}\mathbf{u} = {}^{n}\phi $$

on ${}^{n}\Gamma_U$, where ${}^{n}\phi$ is not necessarily zero. The boundary conditions in terms of stresses and forces are

$$ {}^{n}S_{ij}\,{}^{n}N_j = {}^{n}F_i $$

on ${}^{n}\Gamma_F$. And the boundary conditions for the contact surface, defined by tangental forces and arising from friction, are given by the same general friction function as before

$$ {}^{n}F_T = \mathcal{F}_T. $$

3.3.2 Variational of incremental equation of motion

After expressing the equations describing the problem in incremental form we obtain the updated form of (3.7)

$$\begin{aligned}
&\int_{{}^n\Omega} \left({}^{n+1}S_{kl}\delta_{li} + {}^{n+1}S_{kl}u_{l,i}\right)\left({}^n v_{i,k} + {}^n\dot{u}_{i,k}\right) dV \\
&- \int_{{}^n\Gamma_F} {}^{n+1}F_i\left({}^n v_i - {}^n\dot{u}_i\right) d\gamma - \int_{{}^n\Gamma_U} {}^{n+1}F_i\left({}^n v_i - {}^n\dot{u}_i\right) d\gamma \\
&- \int_{{}^n\Gamma_S} \left\{ {}^{n+1}F_N\left({}^n v_N - {}^n\dot{u}_N\right) + {}^{n+1}\mathcal{F}_T\left({}^n v_T - {}^n\dot{u}_T\right)\right\} d\gamma \\
&+ \int_{{}^n\Omega} {}^{n+1}\rho_0\, {}^{n+1}f_i\left({}^n v_i - {}^n\dot{u}_i\right) dV + \int_{{}^n\Omega} {}^{n+1}\rho_0\, {}^n t_i\left({}^n v_i - {}^n\dot{u}_i\right) = 0, \qquad (3.15)
\end{aligned}$$

for $v_i \in V$, $V \subset \mathcal{H}^2({}^n\Omega)$.

The appropriate constitutive relations for the updated Lagrangian formulation are given, where the hyperoperator for an elastic-plastic material is expressed by

$${}^n\boldsymbol{C}^{\mathrm{EP}} = \boldsymbol{C}^{\mathrm{E}} - \frac{\boldsymbol{C}^{\mathrm{E}}\,{}^n\boldsymbol{q}\left(\boldsymbol{C}^{\mathrm{E}}\,{}^n\boldsymbol{q}\right)^{\mathsf{T}}}{{}^n\boldsymbol{p}^{\mathsf{T}}\,{}^n\boldsymbol{q} + {}^n\boldsymbol{q}^{\mathsf{T}}\boldsymbol{C}^{\mathrm{E}}\,{}^n\boldsymbol{q}}, \qquad (3.16)$$

and components of vectors $\boldsymbol{p}$ and $\boldsymbol{q}$ are given by

$${}^n p_{ij} = -\frac{\partial^n f}{\partial\, {}^n e^{\mathrm{P}}_{ij}} = \left(\frac{2}{3}\,{}^n\sigma_{\mathrm{pl}}\frac{d^n\sigma_{\mathrm{pl}}}{dW^{\mathrm{pl}}}\right){}^n\tau_{ij} = \frac{2}{3}\left(\frac{EE_T}{E - E_T}\right){}^n\tau_{ij}, \qquad (3.17)$$

$${}^n q_{ij} = \frac{\partial^n f}{\partial\, {}^n\tau_{ij}} = {}^n s_{ij}, \qquad (3.18)$$

where f is the yield function. The tangent modulus E_T is specified using the stress-strain curve for the one dimensional tension test. The elastic hyperop-

erator is given in terms of Young's modulus E and Poisson's ratio ν by

$$\boldsymbol{C}^{\mathrm{E}} = \frac{E(1-\nu)}{(1+\nu)(1-2\nu)} \begin{bmatrix} 1 & \frac{\nu}{1-\nu} & \frac{\nu}{1-\nu} & 0 & 0 & 0 \\ \frac{\nu}{1-\nu} & 1 & \frac{\nu}{1-\nu} & 0 & 0 & 0 \\ \frac{\nu}{1-\nu} & \frac{\nu}{1-\nu} & 1 & 0 & 0 & 0 \\ 0 & 0 & 0 & \frac{1-2\nu}{2(1-\nu)} & 0 & 0 \\ 0 & 0 & 0 & 0 & \frac{1-2\nu}{2(1-\nu)} & 0 \\ 0 & 0 & 0 & 0 & 0 & \frac{1-2\nu}{2(1-\nu)} \end{bmatrix}$$

The elastic-plastic hyperoperator is [2]

$$\boldsymbol{C}^{\mathrm{EP}} = \frac{E}{1+\nu} \times$$

$$\begin{bmatrix} \frac{1-\nu}{1-2\nu} - \beta({}^{n}S_{11})^2 & \frac{\nu}{1-2\nu} - \beta\,{}^{n}S_{11}\,{}^{n}S_{22} & \frac{\nu}{1-2\nu} - \beta\,{}^{n}S_{11}\,{}^{n}S_{33} & -\beta\,{}^{n}S_{11}\,{}^{n}S_{12} & -\beta\,{}^{n}S_{11}\,{}^{n}S_{23} & -\beta\,{}^{n}S_{11}\,{}^{n}S_{13} \\ & \frac{1-\nu}{1-2\nu} - \beta({}^{n}S_{22})^2 & \frac{\nu}{1-2\nu} - \beta\,{}^{n}S_{22}\,{}^{n}S_{33} & -\beta\,{}^{n}S_{22}\,{}^{n}S_{12} & -\beta\,{}^{n}S_{22}\,{}^{n}S_{23} & -\beta\,{}^{n}S_{22}\,{}^{n}S_{13} \\ & & \frac{1-\nu}{1-2\nu} - \beta({}^{n}S_{33})^2 & -\beta\,{}^{n}S_{33}\,{}^{n}S_{12} & -\beta\,{}^{n}S_{33}\,{}^{n}S_{23} & -\beta\,{}^{n}S_{33}\,{}^{n}S_{13} \\ & & & \frac{1}{2} - \beta({}^{n}S_{12})^2 & -\beta\,{}^{n}S_{12}\,{}^{n}S_{23} & -\beta\,{}^{n}S_{12}\,{}^{n}S_{13} \\ & \text{symm.} & & & \frac{1}{2} - \beta({}^{n}S_{23})^2 & -\beta\,{}^{n}S_{23}\,{}^{n}S_{13} \\ & & & & & \frac{1}{2} - \beta({}^{n}S_{13})^2 \end{bmatrix},$$

where

$$\beta = \frac{3}{2}\frac{1}{{}^{n}\sigma_{\mathrm{pl}}^2} \Big/ \left(1 + \frac{2}{3}\frac{EE_T}{E-E_T}\frac{1+\nu}{E}\right).$$

3.4 Special Cases of Formulations

The above formulation is the full three dimensional formulation. However, in practice this is very expensive in computational resources. Thus, two special cases which are two dimensional are considered for some of the simulated processes. They are the plane strain case for rolling and the axisymmetric case for hemispherical punching and cup deep-drawing.

3.4.1 Plane strain case

In the case of plane strain the stress and strain tensors have three components, viz., S_{xx}, S_{yy}, S_{xy} and $\varepsilon_{xx}, \varepsilon_{yy}, \varepsilon_{xy}$. The elastic hyperoperator $\boldsymbol{C}^{\mathrm{E}}$ for plane strain is defined as [2]

$$\boldsymbol{C}^{\mathrm{E}} = \frac{E(1-\nu)}{(1-\nu)(1-2\nu)} \begin{bmatrix} 1 & \dfrac{\nu}{1-\nu} & 0 \\ \dfrac{\nu}{1-\nu} & 1 & 0 \\ 0 & 0 & \dfrac{1-2\nu}{2(1-\nu)} \end{bmatrix},$$

The elastic-plastic hyperoperator ${}^{n}\boldsymbol{C}^{\mathrm{EP}}$ suitable for the plane strain has the form [2]

$${}^{n}\boldsymbol{C}^{\mathrm{EP}} = \frac{E}{1+\nu} \begin{bmatrix} \dfrac{1-\nu}{1-2\nu} - \beta\, {}^{n}S_{11}^{2} & \dfrac{\nu}{1-2\nu} - \beta\, {}^{n}S_{11}\, {}^{n}S_{22} & -\beta\, {}^{n}S_{11}\, {}^{n}S_{12} \\ \dfrac{\nu}{1-2\nu} - \beta\, {}^{n}S_{22}\, {}^{n}S_{11} & \dfrac{1-\nu}{1-2\nu} - \beta\, {}^{n}S_{22}^{2} & -\beta\, {}^{n}S_{22}\, {}^{n}S_{12} \\ -\beta\, {}^{n}S_{12}\, {}^{n}S_{11} & -\beta\, {}^{n}S_{12}\, {}^{n}S_{22} & -\beta\, {}^{n}S_{12}^{2} \end{bmatrix}.$$

3.4.2 Axisymmetric case

In the case of axisymmetry, the stress and strain tensors have four components, viz., $S_{rr}, S_{rr}, S_{rz}, S_{\psi\psi}$ and $\varepsilon_{rr}, \varepsilon_{rr}, \varepsilon_{rz}, \varepsilon_{\psi\psi}$. The elastic hyperoperator [2] for the axisymmetric case is

$$C^{\mathrm{E}} = \frac{E(1-\nu)}{(1-\nu)(1-2\nu)} \begin{bmatrix} 1 & \frac{\nu}{1-\nu} & 0 & \frac{\nu}{1-\nu} \\ \frac{\nu}{1-\nu} & 1 & 0 & \frac{\nu}{1-\nu} \\ 0 & 0 & \frac{1-2\nu}{2(1-\nu)} & 0 \\ \frac{\nu}{1-\nu} & \frac{\nu}{1-\nu} & 0 & 1 \end{bmatrix}$$

and the elastic-plastic hyperoperator [2] is

$$C^{\mathrm{EP}} = \frac{E}{1+\nu} \begin{bmatrix} \frac{1-\nu}{1-2\nu} - \beta({}^{n}S_{11})^2 & \frac{\nu}{1-2\nu} - \beta\,{}^{n}S_{11}\,{}^{n}S_{22} & -\beta\,{}^{n}S_{11}\,{}^{n}S_{12} & \frac{\nu}{1-2\nu} - \beta\,{}^{n}S_{11}\,{}^{n}S_{33} \\ & \frac{1-\nu}{1-2\nu} - \beta({}^{n}S_{22})^2 & -\beta\,{}^{n}S_{22}\,{}^{n}S_{12} & \frac{\nu}{1-2\nu} - \beta\,{}^{n}S_{22}\,{}^{n}S_{33} \\ & & \frac{1}{2} - \beta({}^{n}S_{12})^2 & -\beta\,{}^{n}S_{12}\,{}^{n}S_{33} \\ & \text{symm.} & & \frac{1-\nu}{1-2\nu} - \beta({}^{n}S_{33})^2 \end{bmatrix}$$

3.5 Finite Element Discretisation

The contact problem is solved numerically by the finite element method. This involves the discretisation of the variational equation (3.15), which, for a single element e, is given by

$$\begin{aligned} &\left\{ \int_{{}^{n}\Omega^e} [\boldsymbol{B}_L^e]^{\mathsf{T}} \boldsymbol{C}^{\mathrm{EP}} [\boldsymbol{B}_L^e] dV^e + \int_{{}^{n}\Omega^e} [\boldsymbol{B}_{NL}^e]^{\mathsf{T}} \boldsymbol{\tau} [\boldsymbol{B}_{NL}^e] dV^e \right\} \boldsymbol{U} \\ &\quad + {}^{0}\rho \left\{ \int_{{}^{n}\Omega^e} [\boldsymbol{H}^e]^{\mathsf{T}} [\boldsymbol{H}^e] dV^e \right\} \ddot{\boldsymbol{U}} - \int_{{}^{n}\Omega^e} [\boldsymbol{B}_L^e]^{\mathsf{T}} \boldsymbol{\tau}\, dV^e - \int_{{}^{n}\Gamma_F^e} [\boldsymbol{H}_S^e]^{\mathsf{T}} \boldsymbol{F}\, dA^e \\ &\quad + \int_{{}^{n}\Gamma_S^e} [\boldsymbol{H}_S^e]^{\mathsf{T}} \boldsymbol{F}_N\, dA^e - \int_{{}^{n}\Gamma_S^e} \lambda [\boldsymbol{H}_S^e]^{\mathsf{T}} \boldsymbol{\mathcal{F}}_T\, dA^e = 0 \end{aligned} \tag{3.19}$$

where: $[\boldsymbol{H}^e]$ is the matrix of volume interpolation functions,
$[\boldsymbol{H}_S^e]$ is the matrix of surface interpolation functions,
$[\boldsymbol{B}_L^e]$ is the linear strain-displacement transformation matrix,
$[\boldsymbol{B}_{NL}^e]$ is the nonlinear strain-displacement transformation matrix,
$\boldsymbol{C}^{\mathrm{EP}}$ is the stress-strain elastic-plastic matrix, and
λ is a Lagrange multiplier for the frictional contact constraints.

For the three dimensional case those matrices are given by:

$$[\boldsymbol{B}_L^e] = \begin{bmatrix} h_{1,1} & 0 & 0 & h_{2,1} & \cdots & 0 \\ 0 & h_{1,2} & 0 & 0 & \cdots & 0 \\ 0 & 0 & h_{1,3} & 0 & \cdots & h_{N,3} \\ h_{1,2} & h_{1,1} & 0 & h_{2,2} & \cdots & 0 \\ 0 & h_{1,3} & h_{1,2} & 0 & \cdots & h_{N,2} \\ h_{1,2} & 0 & h_{1,1} & h_{2,3} & \cdots & h_{N,1} \end{bmatrix} \tag{3.20}$$

$$[\boldsymbol{B}_{NL}^e] = \begin{bmatrix} \tilde{\boldsymbol{B}} & & \\ & \tilde{\boldsymbol{B}} & \\ & & \tilde{\boldsymbol{B}} \end{bmatrix} \qquad \tilde{\boldsymbol{B}} = \begin{bmatrix} h_{1,1} & 0 & 0 & h_{2,1} & \cdots & h_{N,1} \\ h_{1,2} & 0 & 0 & h_{2,2} & \cdots & h_{N,2} \\ h_{1,3} & 0 & 0 & h_{2,3} & \cdots & h_{N,3} \end{bmatrix} \tag{3.21}$$

where the h_a, $a = 1, \ldots, N$ are the interpolation functions, N is the number of nodes, $h_{a,i} = \partial h / \partial x_i$, $i = 1, 2, 3$, and blank entries in the matrices are zero.

Assembling the complete FE system consists of summing over all the elements [25]:

$$\begin{aligned} &\sum_e \left\{ \int_{n\Omega^e} [\boldsymbol{B}_L^e]^{\mathsf{T}} \boldsymbol{C}^{\mathrm{EP}} [\boldsymbol{B}_L^e] dV^e + \int_{n\Omega^e} [\boldsymbol{B}_{NL}^e]^{\mathsf{T}} \boldsymbol{\tau} [\boldsymbol{B}_{NL}^e] dV^e \right\} \boldsymbol{U} \\ &\quad + \sum_e {}^0\rho \left\{ \int_{n\Omega^e} [\boldsymbol{H}^e]^{\mathsf{T}} [\boldsymbol{H}^e] dV^e \right\} \ddot{\boldsymbol{U}} - \sum_e \int_{n\Omega^e} [\boldsymbol{B}_L^e]^{\mathsf{T}} \boldsymbol{\tau} \, dV^e - \sum_e \int_{n\Gamma_F^e} [\boldsymbol{H}_S^e]^{\mathsf{T}} \boldsymbol{F} \, dA^e \\ &\quad + \sum_e \int_{n\Gamma_S^e} [\boldsymbol{H}_S^e]^{\mathsf{T}} \boldsymbol{F}_N \, dA^e - \sum_e \int_{n\Gamma_S^e} \lambda [\boldsymbol{H}_S^e]^{\mathsf{T}} \boldsymbol{\mathcal{F}}_T \, dA^e = 0 \end{aligned} \tag{3.22}$$

which can simply be rewritten as:

$$\boldsymbol{M}\ddot{\boldsymbol{U}} + \boldsymbol{K}\boldsymbol{U} = \boldsymbol{R} \tag{3.23}$$

where $\boldsymbol{M}$ is the mass matrix given by

$$\boldsymbol{M} = \sum_e {}^0\rho \int_{{}^n\Omega^e} [\boldsymbol{H}^e]^\mathsf{T} [\boldsymbol{H}^e] dV^e,$$

$\boldsymbol{K}$ is the stiffnes matrix composed of a linear and a nonlinear part

$$\boldsymbol{K} = \boldsymbol{K}_L + \boldsymbol{K}_{NL}$$

given by

$$\begin{aligned} \boldsymbol{K}_L &= \sum_e \int_{{}^n\Omega^e} [\boldsymbol{B}_L^e]^\mathsf{T} \boldsymbol{C}^{\mathrm{EP}} [\boldsymbol{B}_L^e] dV^e \\ \boldsymbol{K}_{NL} &= \int_{{}^n\Omega^e} [\boldsymbol{B}_{NL}^e]^\mathsf{T} \boldsymbol{\tau} [\boldsymbol{B}_{NL}^e] dV^e, \end{aligned}$$

and $\boldsymbol{R}$ is the right-hand side matrix of forces composed of initial forces, body forces and surface forces,

$$\boldsymbol{R} = \boldsymbol{R}_I + \boldsymbol{R}_B + \boldsymbol{R}_S$$

given by

$$\begin{aligned} \boldsymbol{R}_I &= \sum_e \int_{{}^n\Omega^e} [\boldsymbol{B}_L^e]^\mathsf{T} \boldsymbol{\tau} \, dV^e \\ \boldsymbol{R}_B &= \sum_e \int_{{}^n\Gamma_F^e} [\boldsymbol{H}_S^e]^\mathsf{T} \boldsymbol{F} \, dA^e \\ \boldsymbol{R}_S &= \sum_e \int_{{}^n\Gamma_S^e} [\boldsymbol{H}_S^e]^\mathsf{T} \boldsymbol{F}_N \, dA^e + \sum_e \int_{{}^n\Gamma_S^e} \lambda [\boldsymbol{H}_S^e]^\mathsf{T} \boldsymbol{\mathcal{F}}_T \, dA^e. \end{aligned}$$

Chapter 4

Results

For the numerical experiment part of this work parameters were chosen for the friction models from experimental measurements. The dimensions of the processes were selected from standard problems.

The processes are simulated within the FEM using the program ABAQUS, which allows the use of a user subroutine FRIC which completely defines the frictional stresses and slips on the contact surface interface. Therefore each friction model was coded in FORTRAN as the subroutine FRIC which is called by ABAQUS for each contact point. The subroutine returns the friction stresses and slips, and the necessary derivative information for the Jacobian of the Newton iteration scheme for the solution of the nonlinear FEM equations.

First the values for the friction parameters are given, then the dimensions and material properties for the processes. The results for the friction-process combinations are listed, together with comments.

4.1 Friction parameters

4.1.1 Amontons-Coulomb

For the metalworking processes investigated the workpiece is usually lubricated and the measured coefficient of friction is between 0.08–0.20 [5, 11] for contact between hard (tool) steel and mild steel. For dry contact the measured figures are between 0.50–1.00 [11]. The chosen values are:

Coefficient of friction:		μ
	dry	0.80
	lubricated	0.15

4.1.2 WVS

For dry contact the parameters α and β can be calculated from equations (2.16) and (2.19) using experimental data [14, 39]. For lubricated contact the parameters are estimated.

dry (from calculation)	α	0.0906
	β	0.189
lubricated (estimated)	α	0.03
	β	0.15
for dry and lubricated (from [38])	ν	0.80

4.1.3 QSS

Using the recommended method of calculation in [40] and the values found for χ in [41][1] for dry contact, the values for equation (2.25) are:

[1] In [40, 41] the quantity χ is called β.

shear strength	S_1, S_2	251	167	Mpa
proportion of asperity ploughing	χ	0.60		
area of asperity contacts	A_a	0.0513		mm^2
area of debris contacts	A_{d1}, A_{d2}	0.0196	0.0245	mm^2
hardness of materials	H_1, H_2	1000	800	MPa
shear stress of adhesion	τ_{a1}, τ_{a2}	1.12	1.12	MPa

4.1.4 Wilson lubricant

For the Wilson model the parameters are:

viscosity	η	0.0005	MPa s
tool roughness	σ_1	34	nm
work piece roughness	σ_2	40	nm
asperity half-spacing	l	2.23	μm
asperity slope	θ_t	0.14	
shear strength	S	167	MPa
adhesion coefficient	k	0.25	

4.2 Process parameters

All the material data for the different process simulations are given in table 4.1. These data were chosen to conform to established practice: the data are for steels commonly used in the processes simulated. The data for deep drawing was taken from a technical report describing experimental measurements [30].

4.2.1 Punching

The mesh for the hemispherical punch is given in figure 4.1. In this process a hemisphere of diameter 0.2 m indents a steel disk of radius 0.6 m and thickness 0.3 m. The disk was descretised by 135 solid axisymmetric elements with reduced integration. The punch is modelled as a rigid surface. The mesh used is given by figure 4.1.

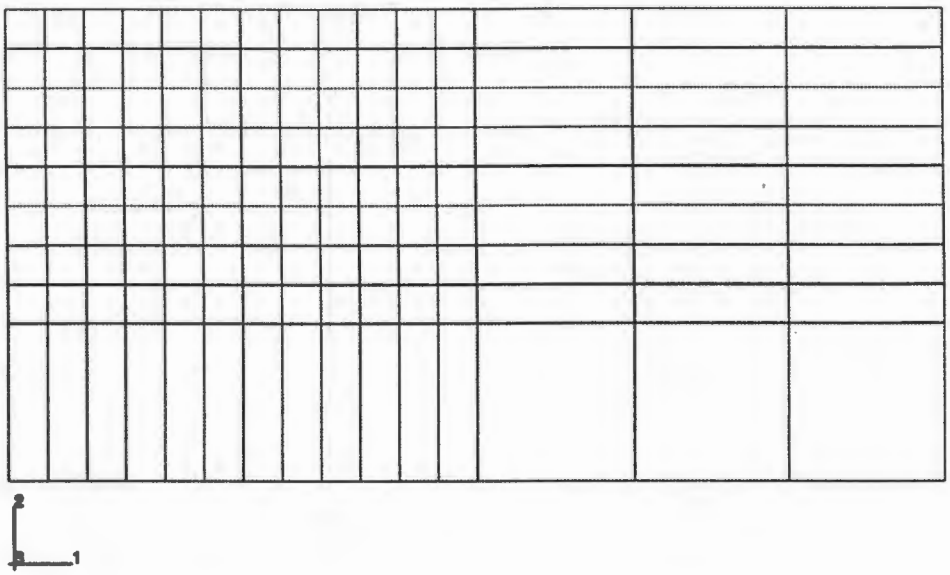

Figure 4.1: The element mesh for the hemispherical punching simulation. The elements are solid axisymmetric with reduced integration.

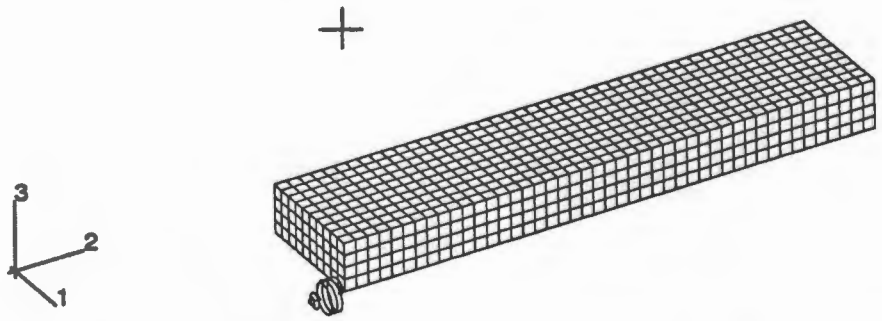

Figure 4.2: The element mesh for the three-dimensional rolling simulation, showing the spring and the centre of the roller.

Process	Young's modulus E (Pa)	Poisson's ratio ν	Plastic yield Y_0 (Pa)	Hardening κ
Punching	2.0×10^{11}	0.30	4.11×10^{8}	0.20
Rolling	2.1×10^{11}	0.30	3.6×10^{8}	0.07
Deep drawing	4.47×10^{11}	0.30	2.44×10^{8}	*

Table 4.1: The material parameters for the processes simulated.

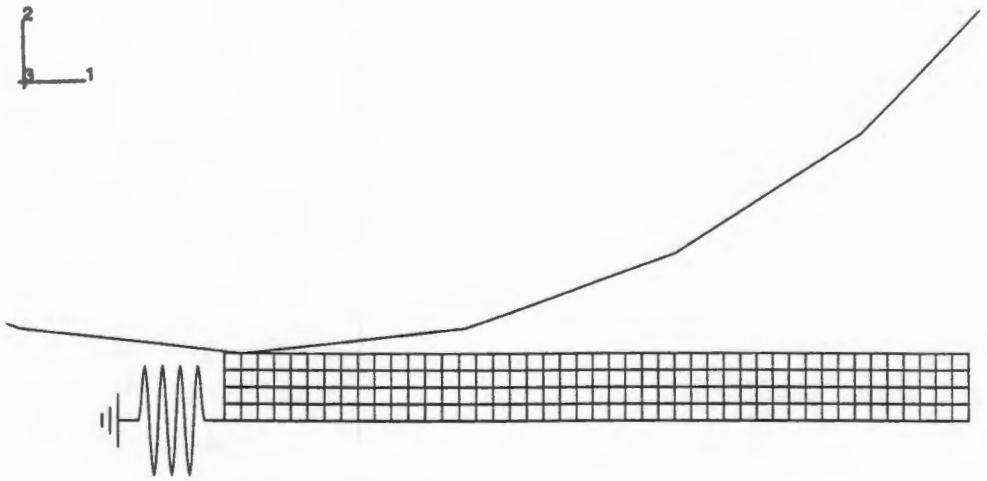

Figure 4.3: The element mesh for the plane strain rolling simulation, showing the spring and the roller.

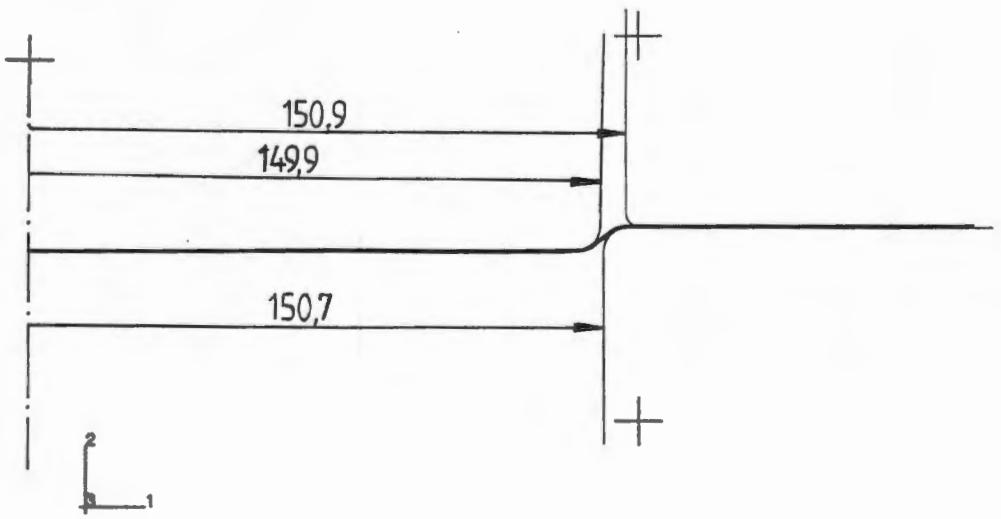

Figure 4.4: The dimensions and boundary conditions for the axisymmetric cup deep drawing simulation.

4.2.2 Rolling

The mesh for the 3D rolling simulation is shown in figure 4.2. The strip of steel is descretised as 1800 solid 3D elements with reduced integration. The symmetry of the process allows one quarter to be used, with appropriate boundary conditions on the inner surfaces. The roller is modelled as a rigid cylinder. The strip has length 225 mm, half width 100 mm and half thickness of 20 mm. The roller has radius 300 mm.

The plane strain 2D rolling simulation is illustrated by figure 4.3. The strip mesh consists of 180 plane stain elements. The symmetry of the problem means that only half of the strip need be modelled with an appropraite boundary condition on the inner side. The roller is modelled as a rigid circle. The strip has length 225 mm and thickness 20 mm. The roller has a radius of 300 mm.

For both it was necessary to restrain the strip at one node with a soft spring. This was chosen rather than the usual restraint of fully fixing one node because the fixed node results in a very large reaction force at the fixed node. The spring only affects a small portion of the solution.

4.2.3 Axisymmetric cup deep drawing

For this simulation the parameters and dimensions were chosen to match the series of experiments done by Sosnowski, et al. [30]. This simulation was thus much more complicated than the others as it used three separate rigid bodies for the three tools. Figure 4.4 shows the geometry for the deep drawing simulation. The blank is descretised using 3000 solid axisymmetric elements in three layers. The die, blank holder and punch are represented by rigid surfaces.

In the report the following fit was made for the stress-strain curve of the metal blanks used

$$\sigma = 320 - 80\exp\left(-7.5\varepsilon^{0.97}\right) \tag{4.1}$$

and other parameters were:

blank radius	250	mm
punch radius	149.9	mm
punch rounding	6.0	mm
die radius	150.7	mm
die roundings	6.0	mm
initial average thickness	0.675	mm
blankholder force	186995	N
punch displacement	6.4	mm

4.3 Results

All the results will be given here. Comments will be made on the solution: convergence, computational times, etc.; and on the resultant values: friction vs pressure, slip, position, etc. The Mises contours for each result will be given, with the results for the four friction models on one figure to allow instant comparison. Also shown will be contour lines for the plastic yield and maximum stress.

4.3.1 Punching

The AC & QSS graphs in figure 4.5 are similar with small noticable variations in the position of the contours. In the QSS case a small island of higher stress appears near the surface upflow of metal. The contours deeper in are very similar to AC. The WVS model differs a lot: the layer of highest stress is the narrowest of the four models. The shapes of the deeper contours are similar to AC & QSS but the overall stresses are lower: hence energy is lower. This is from the large plastic flow of metal on the surface under the punch. As can be seen, the extreme nature of this problem has magnified the differences. The plastic yield contour is shown in figure 4.6. The higher stress line shows clearly the movement under the punch, as does the deformed mesh. The QSS & WVS results show greater surface movement—a result of these models having more surface slip. The plastic yield contour is concave for all models, but is smaller in area for QSS & WVS. In AC & QSS there is the yield region around the upflow of metal at the edge of the punch. In WVS the yielding area is much

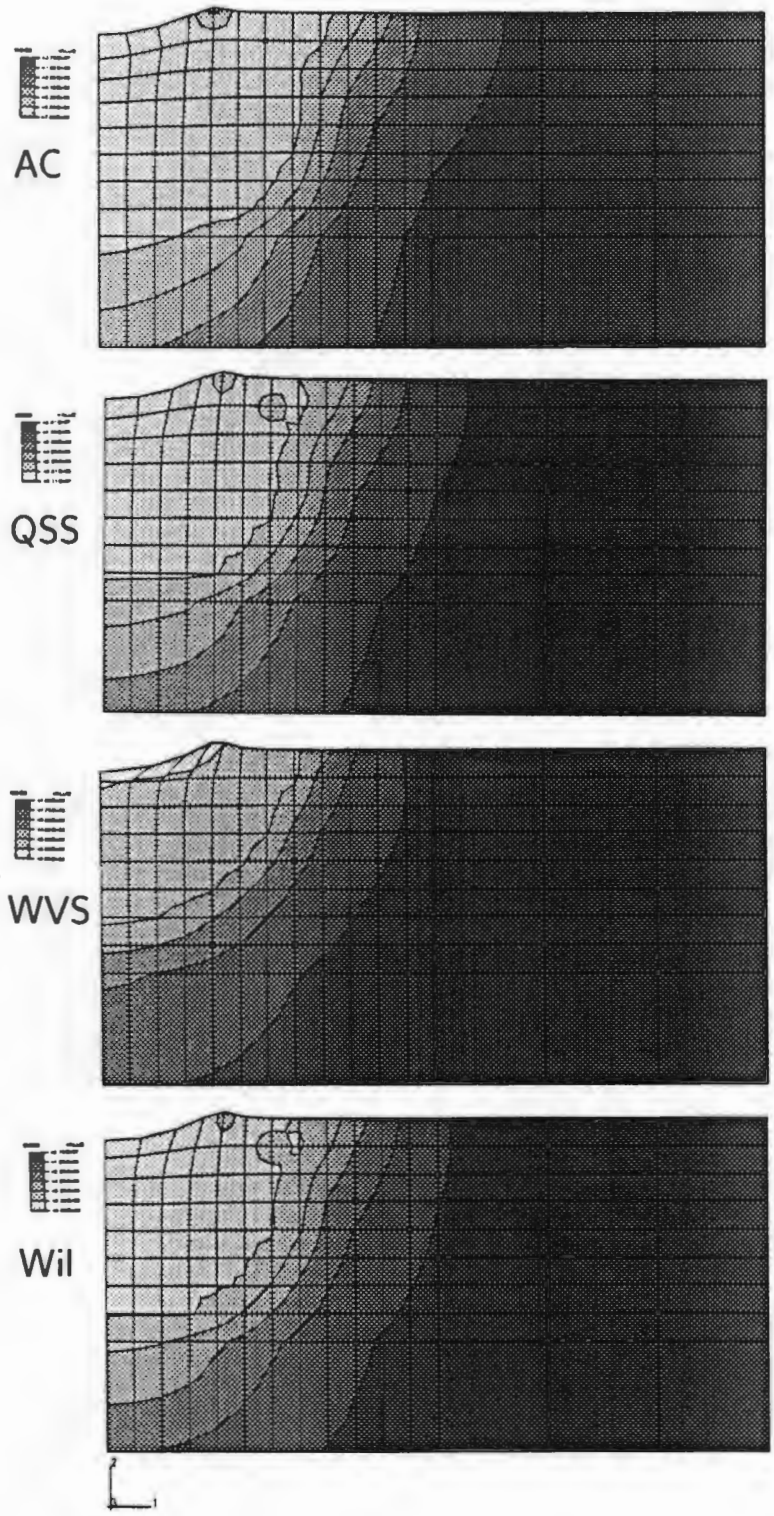

Figure 4.5: The Mises stress contours for the punching simulation.

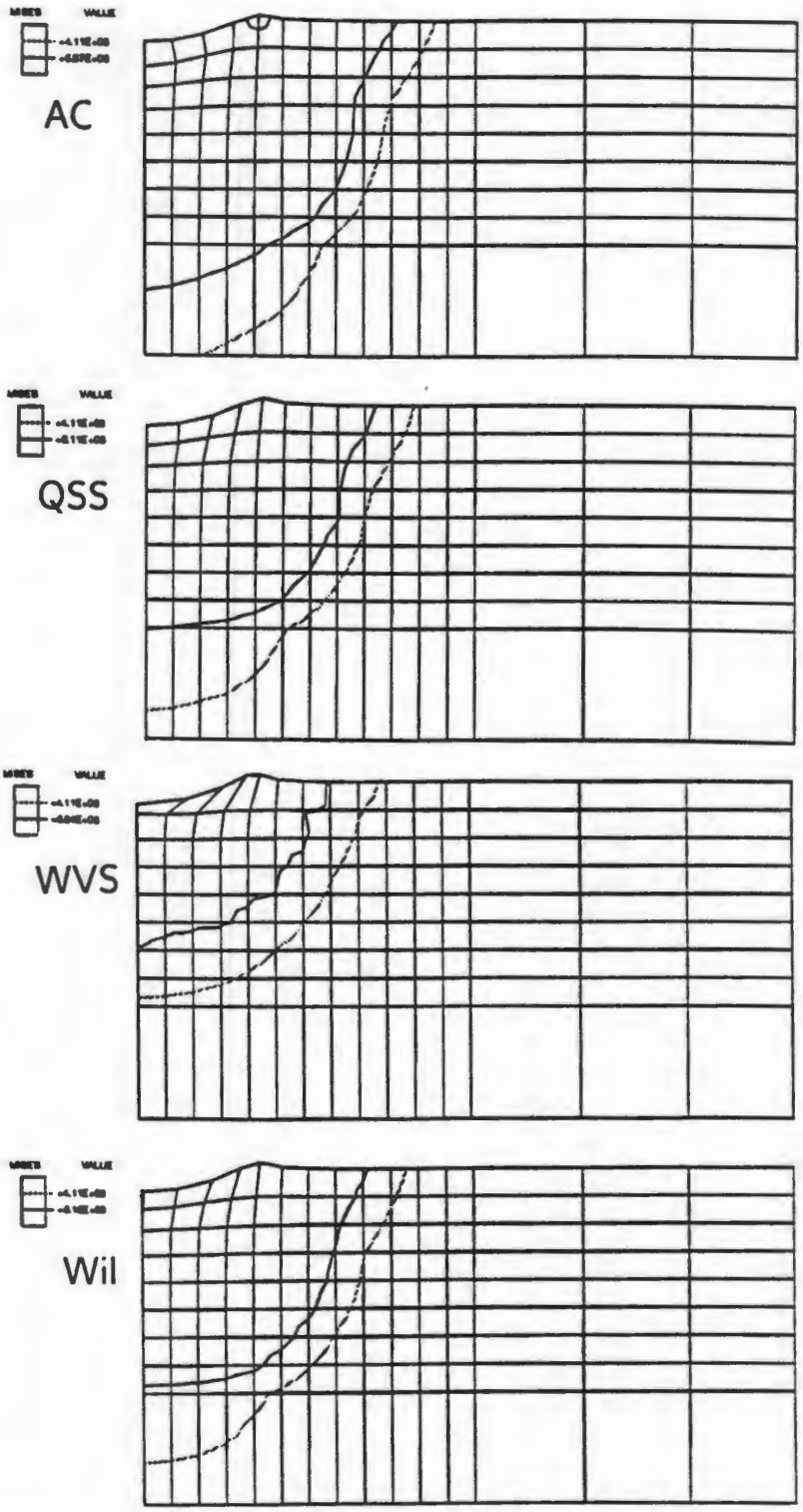

Figure 4.6: The plastic yield contour for the punching simulation.

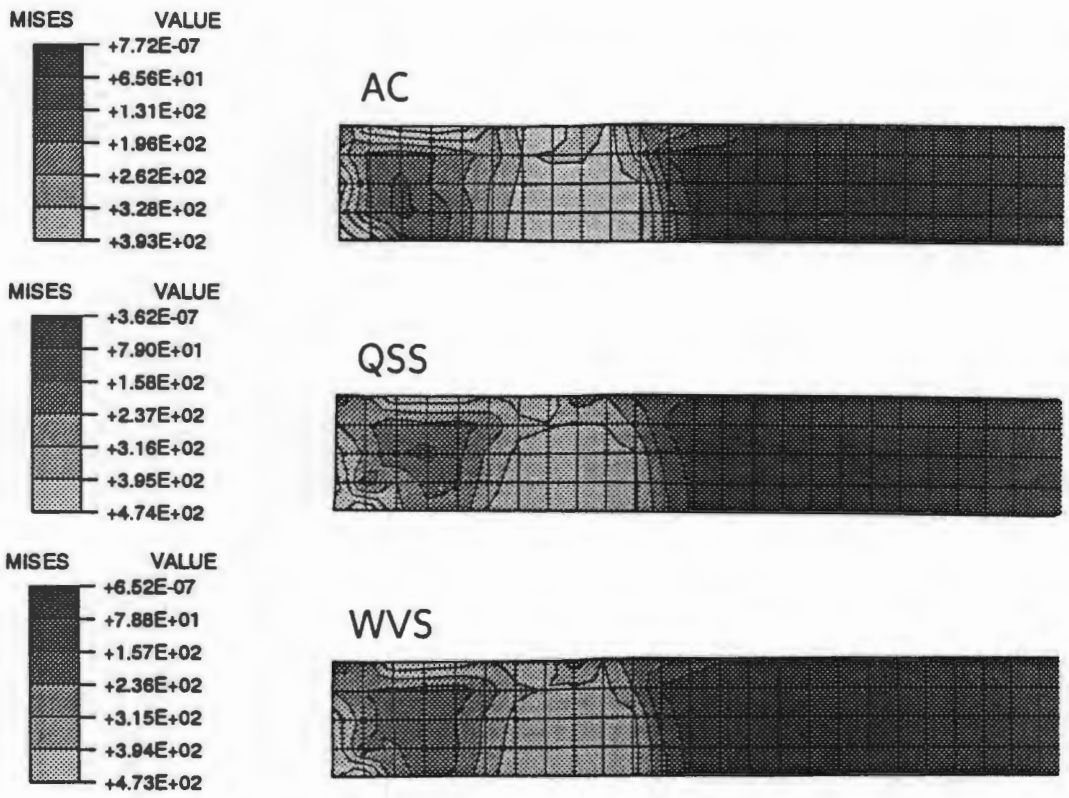

Figure 4.7: The Mises stress contours for the plane strain rolling simulation.

is much smaller and mostly under the punch: the deformation of the punch impact is not distributed deeply here. The Wilson shows more slip under the punch than the AC and QSS models, but less than the WVS model. The stress contours are more like those of the AC and QSS models. As pressures are high in this process, the lubricant would be squeezed thin and so mostly boundary or mixed film states would exist. Then the stresses would be more like the dry models, which allow greater slip, especially the QSS model which has a typically lower stress during sliding.

4.3.2 Rolling

Plane strain rolling simulation

Figure 4.7 shows the Mises stress contours for the plane strain rolling simulations of the different friction models. All material parameters are the same,

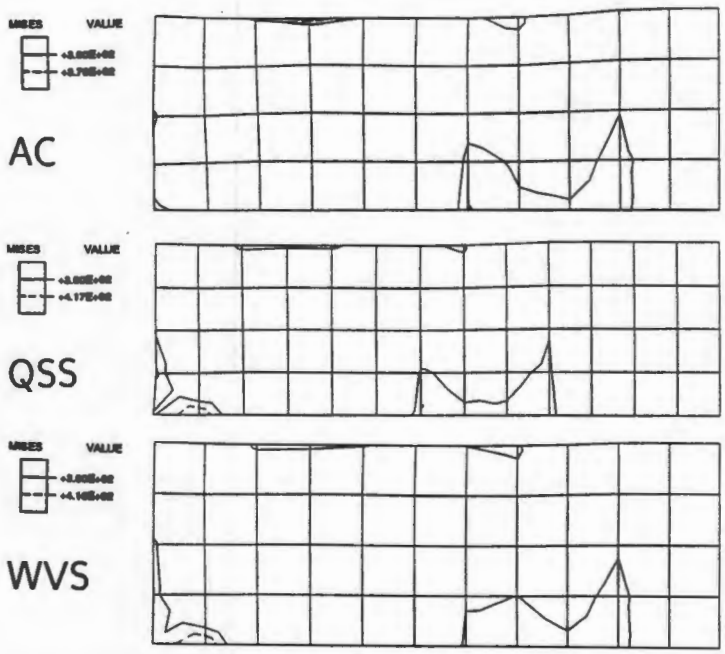

Figure 4.8: The plastic yield contours for the plane strain rolling simulation.

only the friction models differ. The roller has rolled a distance of 25 mm at a depth of 0.5 mm.

As can be seen, the Mises contours differ markedly in shape and value. The legend indicates the maximum and minimum values for the contours. The maximum stresses vary between models.

In figure 4.8 the plastic yield contours are plotted. A small amount of plastic flow occurs around the edge constrained by a spring. This indicates that it would be preferrable to remove the spring. However, this area of yield is small and does not extend into the work region.

Examining the contour lines lying under the surface that has been compressed by the roller it can be seen that the different friction models give rise to different shapes. The AC model has an even spread of plastic deformation just under the rolled surface. The other models show greater irregularities. In the WVS model plastic deformation has occured over a wider area. This is caused by the higher friction stresses, in comparison to the AC model, at the lower pressures generated by the roller moving off the rolled region. In contrast to AC the frictional stresses are lower at the higher pressures generated directly under

the roller. In the QSS case the region of plastic flow is smaller. The QSS model produces much lower friction during slipping, and this shows up as the smaller amount of energy which is transferred from the roller to the material as more is lost during the sliding motion between the roller and strip.

3D rolling simulation

Corresponding to the plane strain rolling simulation there is the full 3D rolling simulation for figures 4.9–4.12.

The Mises stress contours for the three friction models AC, QSS and WVS are shown in figure 4.9. The Wilson model was not implemented for rolling. The region under the roller appears the same for the three models. Examining the region that has been rolled and is now behind the roller shows some difference between models. The AC and QSS models are almost similar, but the QSS model shows higher stress. Also, below the rolled surface the stress is higher. The WVS model result shows much higher distribution of stress on the surface, but lower stress below the roller. This is similar to the punching results which indicate that the WVS model allows greater amount of slip at higher frictional stresses than other models.

The main difference of figure 4.9 is in the region of low stress. Along the leading edge the WVS model shows lower stresses than the AC and QSS models, which are similar. On the inner edge the situation is the same. This is in contrast to the higher stresses seen for WVS on the surface which is rolled, compared to AC and QSS.

Examining the under surface of the strip in figure 4.10, the higher stress distributions are very similar. The differences appear in the region of lower stress: the AC and QSS results are almost identical, but the WVS model shows some small difference in the shape and size of the minimum stress region. We can conclude that surface conditions have little effect on the lower layers.

Figure 4.11 is devoted to showing the plastic yield contour on the upper side of the rolled strip. The area of plastic yielding is similar for AC and QSS, but larger for WVS.

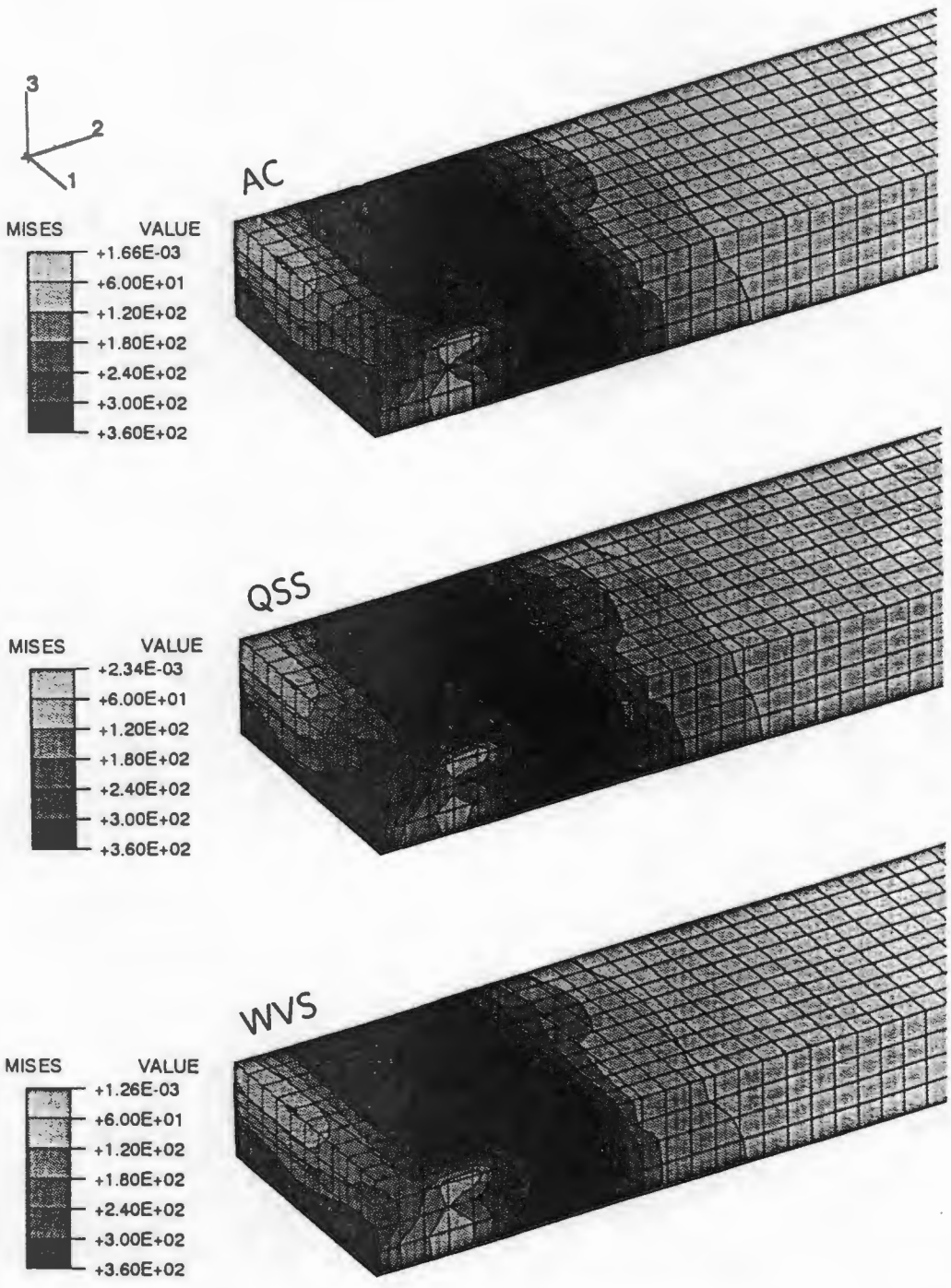

Figure 4.9: The Mises stress contours for the 3D rolling simulation. This is the top of the strip.

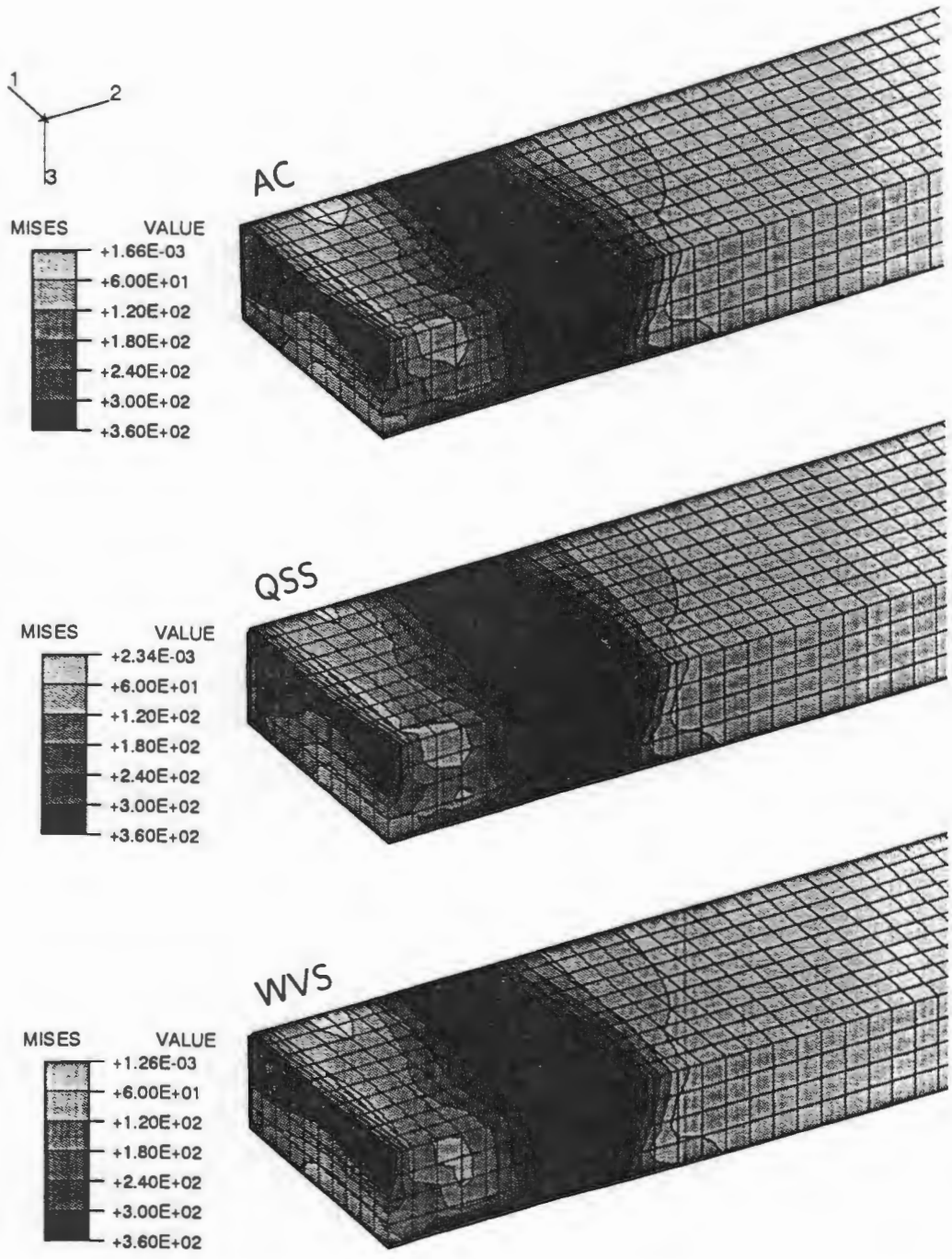

Figure 4.10: The Mises stress contours for the 3D rolling simulation. This is the bottom of the strip.

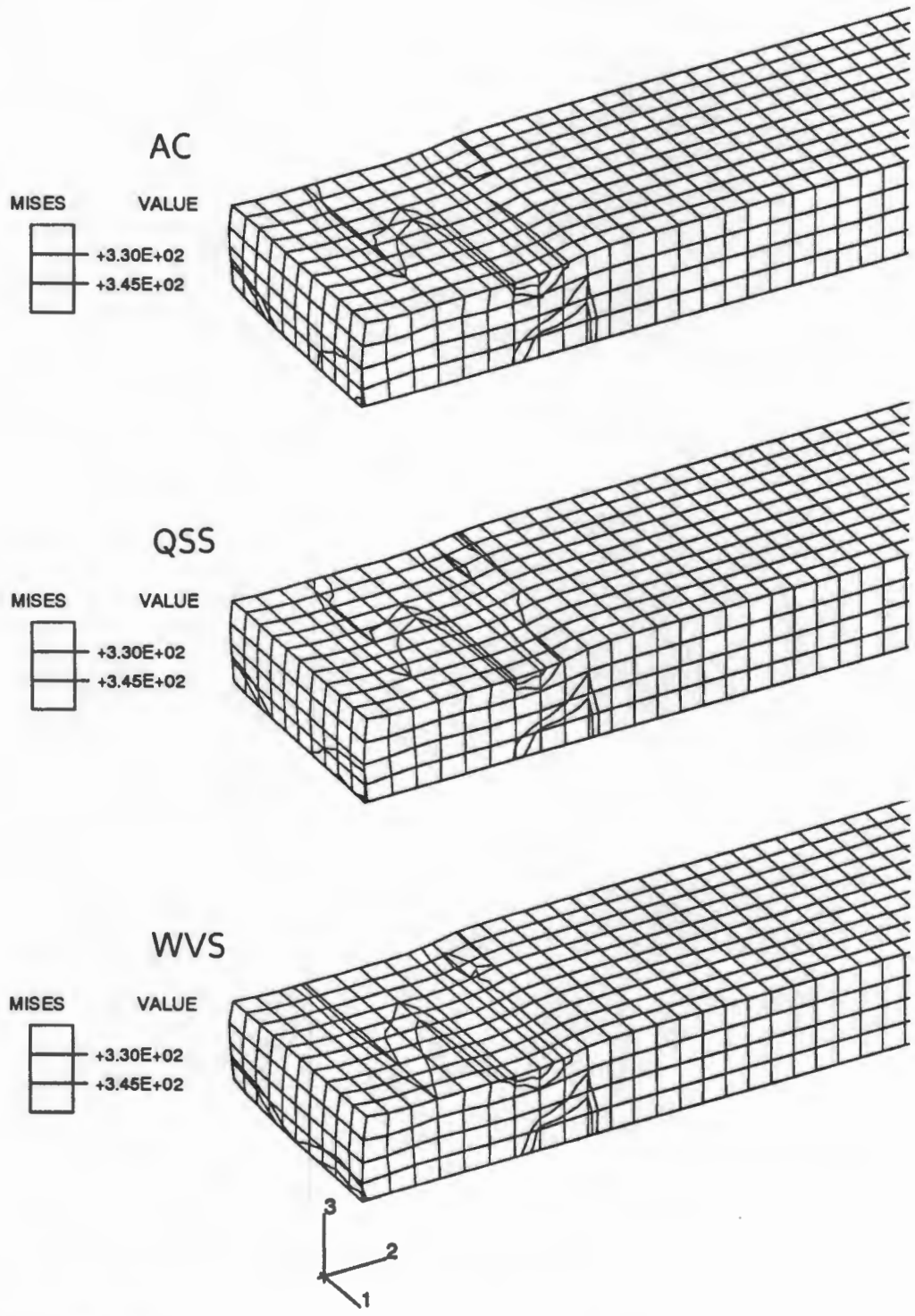

Figure 4.11: The plastic yield contours for the 3D rolling simulation. This is the top of the strip.

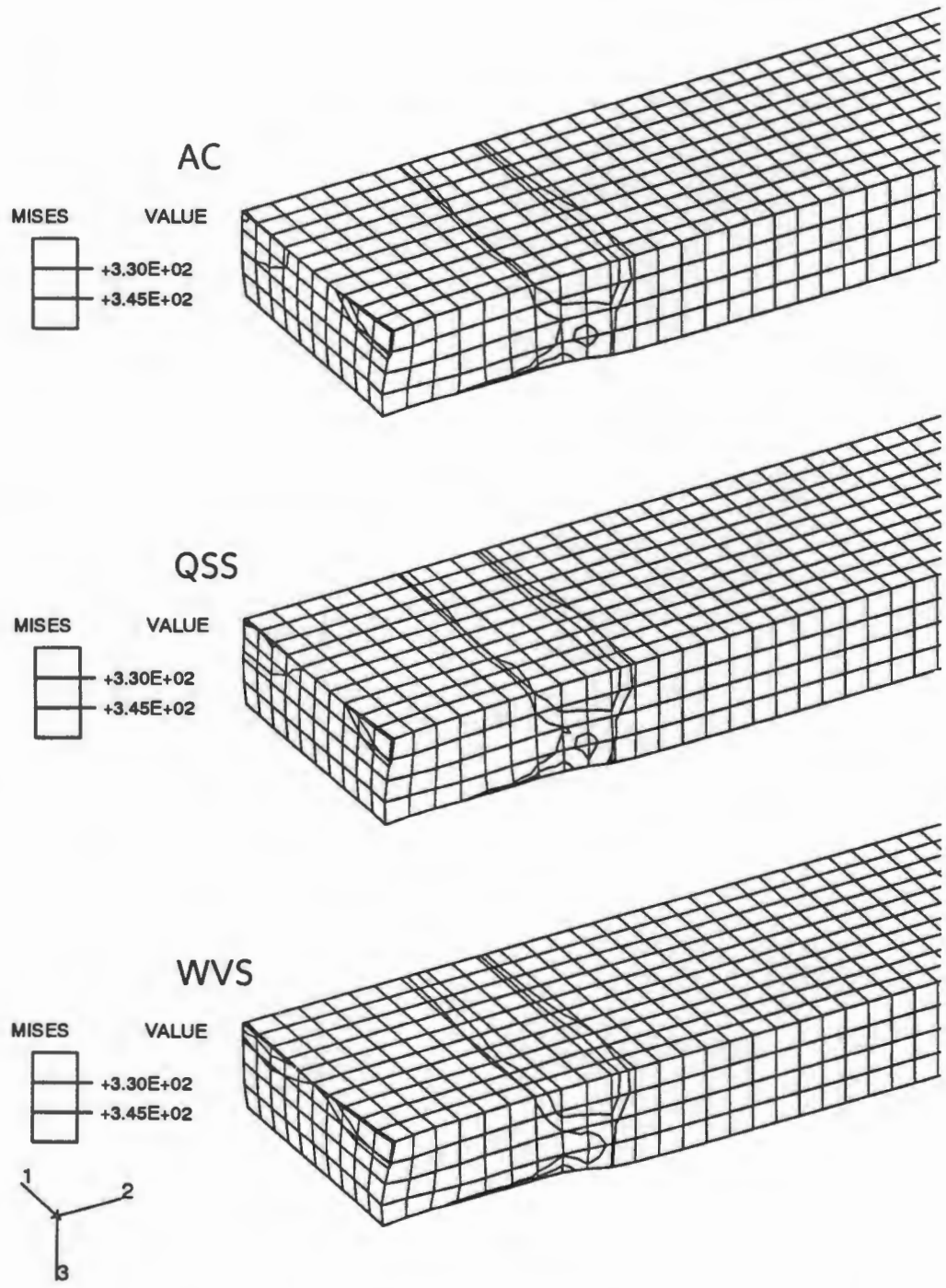

Figure 4.12: The plastic yield contours for the 3D rolling simulation. This is the bottom of the strip.

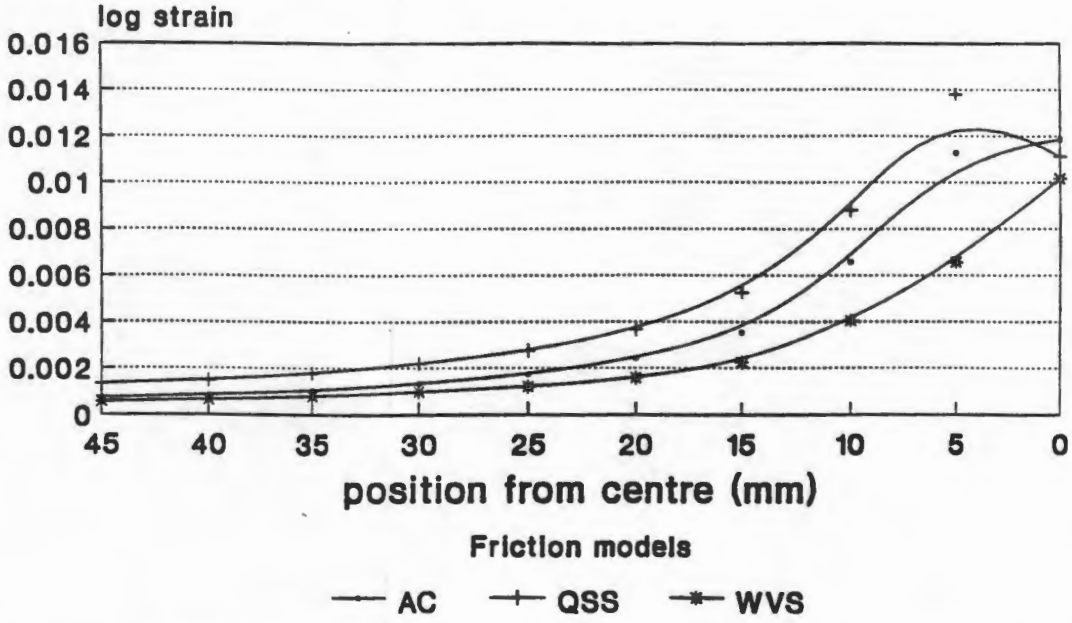

Figure 4.13: Principle strain (ε_{xx}) curves for the 3D rolling simulation. The values are logarithmic strain for the row of elements on the top layer along the roller. This is the region that has been rolled and is still under the roller. The position is measured from the centre of the strip, so that the 45 mm ordinate is the free edge.

In figure 4.12 we have the plastic yield contour for the under surface of the strip. The small island which appears on the free edge in the AC and QSS results shows a region on the verge of yielding. In the WVS result this region has yielded. Thus, from figures 4.11–4.12 we see greater displacements for WVS than for AC and QSS.

To quantify the above discussion table 4.2 shows the minimum and maximum values of the principle stresses for the three friction models.

Figure 4.13 show the strain across the width of the roller on the surface at 25 mm which is just under the axis of the roller. As can be seen, the strain values are small, but show differences between models: The QSS model has a maximum at 5 mm from the centre of the strip. This shows that there is a slipping region which is allowing material to move sideways. This movement of material is less for the AC and WVS models.

Figure 4.14 show the strain lengthwise along the upper layer of elements at the inner edge. The results are almost identical for the three models. The

		S_{11}	S_{22}	S_{33}
AC	max	319.3	385.3	398.5
	min	−491.4	−397.1	−716.9
QSS	max	358.8	377.7	395.2
	min	−483.8	−425.8	−719.0
WVS	max	277.4	399.4	412.7
	min	−482.1	−390.7	−707.2

Table 4.2: The maximum and minimum values of the principle stresses (in MPa) for the 3D rolling simulation.

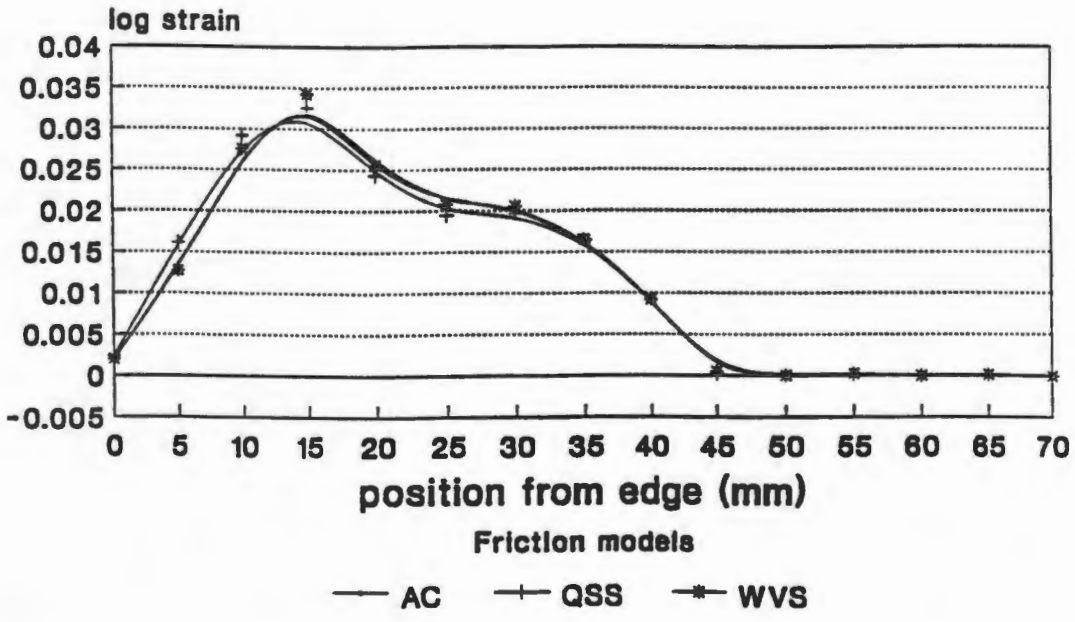

Figure 4.14: Principle strain (ε_{yy}) curves for the 3D rolling simulation. The values are logarithmic strain for the row of elements on the top layer along the inner edge. This is the region that has been rolled. The position is measured from the front edge of the roller.

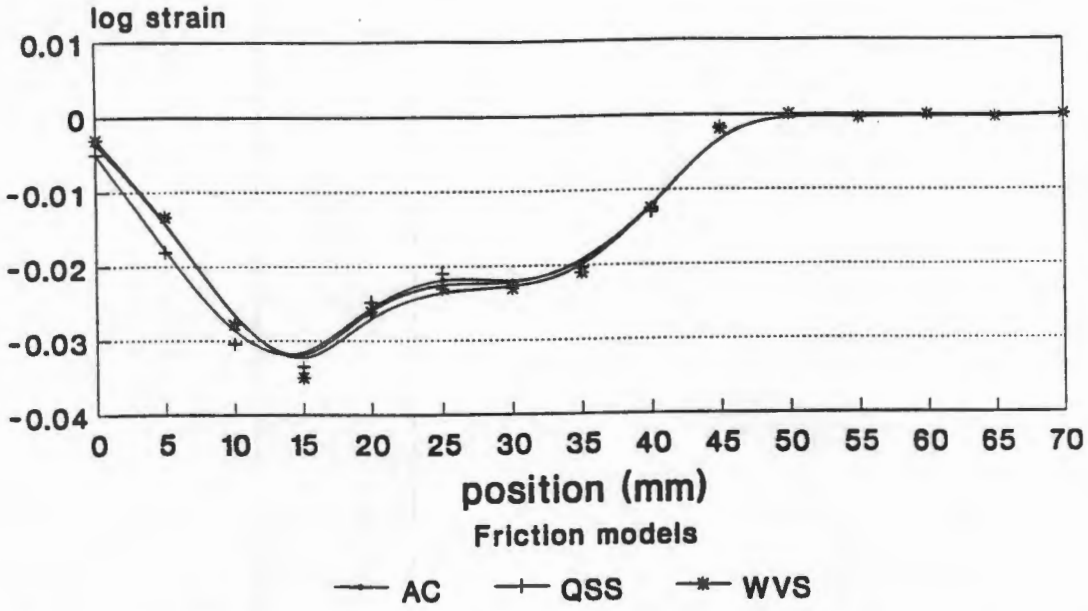

Figure 4.15: Thickness strain (ε_{zz}) curves for the 3D rolling simulation. The values are logarithmic strain for the row of elements on the top layer along the inner edge. This is the region that has been rolled. The position is measured from the front edge of the roller.

peak occurs at 15 mm where material is now leaving the contact region and is pushed backwards. The WVS and AC models show higher values of strain, hence there is more flow away from the roller, and so more slipping along the back edge of the roller.

Figure 4.15 shows the thickness strain along the centre of the upper layer of elements. The horizontal axis shows the distance from the leading edge of the strip. At 15 mm there is the most negative strain; this is the region of material just behind the roller, and so has been rolled and released. Then there is a plateau at 25 mm to 35 mm which is the region currently under the roller. The strain then rises up along the front of the roller to zero where the material is unrolled. There is little difference between the models: The WVS model shows more strain, hence more movement of material, the QSS and AC models are very similar.

4.3.3 Deep drawing

As the blank has such large radius compared to its thickness we concentrate on the important region where the blank bends over the die and punch. There are two areas of interest here: the contact between punch and blank, and the contacts between blank holder, die and blank. The blank was drawn a depth of 6.4 mm as per the experiment in [30]. Firstly the Mises contours for the four friction models are given in figure 4.16, and then the plastic yield contours are displayed in figure 4.17.

Figure 4.16 shows the Mises stress contours for the upper and lower bends of the blank. At the lower bend there is a dividing region between two broad bands of high stress. This region of lower stress is smaller in size for the QSS and WVS models compared to the AC and Wilson model. At the upper bend the high stress region on the outer part of the bend differs for the four models. The AC model is the smallest of the set. The QSS and WVS have identically sized regions, but the Wilson is smaller. In contrast, the Wilson model shows lower stresses which are almost the same as the AC model, which has a coefficient of friction measured from a lubricated surface.

Figure 4.17 shows the plastic yield contours for the deep drawing simulation. The graphs are basically similar with the largest difference occuring for the yield contour in the upper bend. The regions of yielding differ in size: the largest area occurring in the AC model, the least in the Wilson. We can see that the AC model has more plastic yielding, but lower overall stresses then the others. The Wilson model has least yielding and least overall stress. There are two regions of yield on either side of the lower bend, in contrast to the single region of the upper bend. The presence of islands of yielding in the QSS and WVS models indicates higher friction stresses under the blankholder and die. In the lower bend over punch the differences are slight and mainly appear in the higher than yield stress contour.

In order to quantify these differences examine table 4.3, which shows the maximum and minimum principle stresses for the AC and Wilson models. It shows that the stresses for AC are higher than for Wilson. Clearly, the effect of a lubricant is to reduce the stresses in the blank overall.

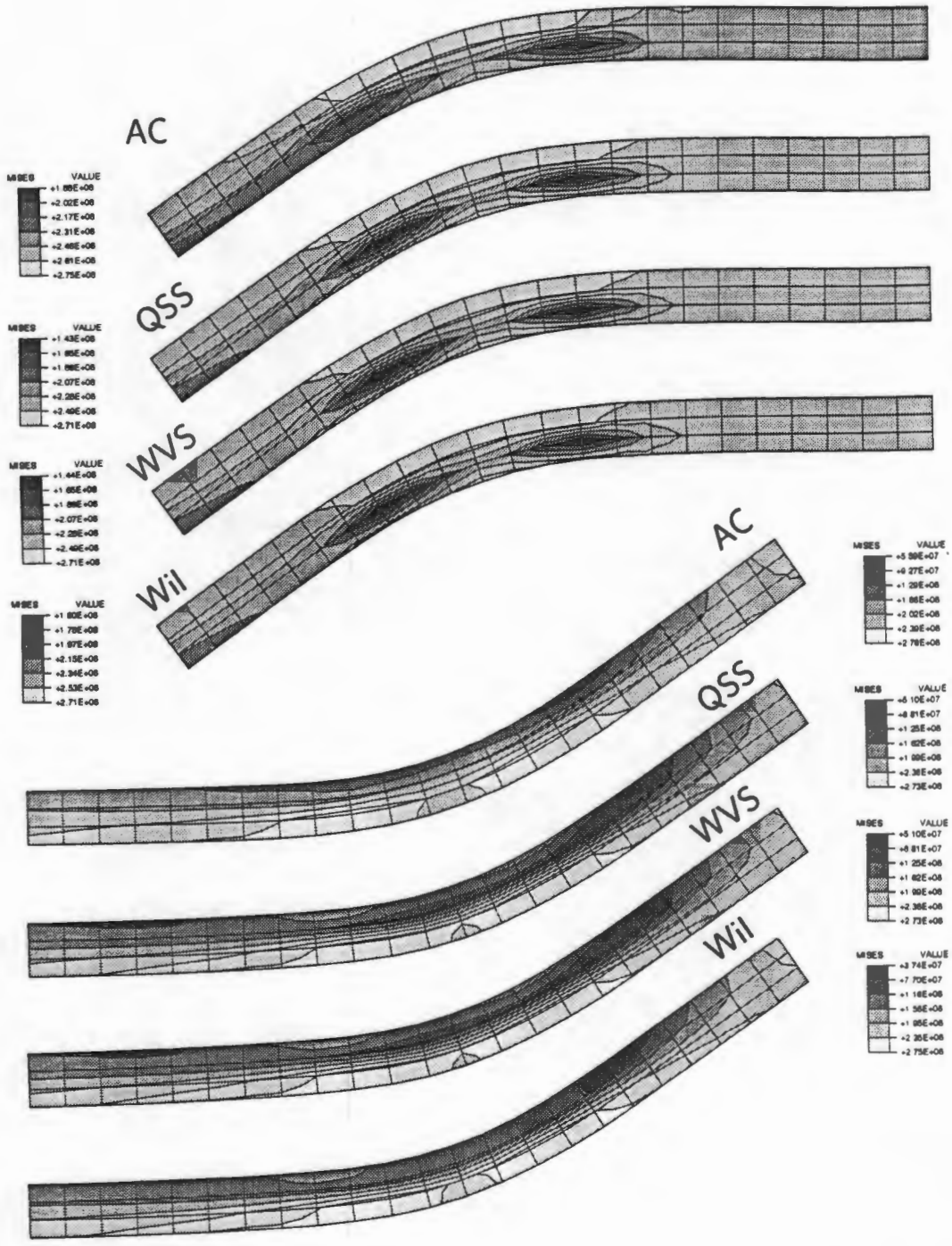

Figure 4.16: The Mises stress contours for the axisymmetric cup deep drawing process for the four friction models. Only the flange of the cup is shown, which is divided into the lower bend under the punch (lower set) and the upper bend over the die (upper set).

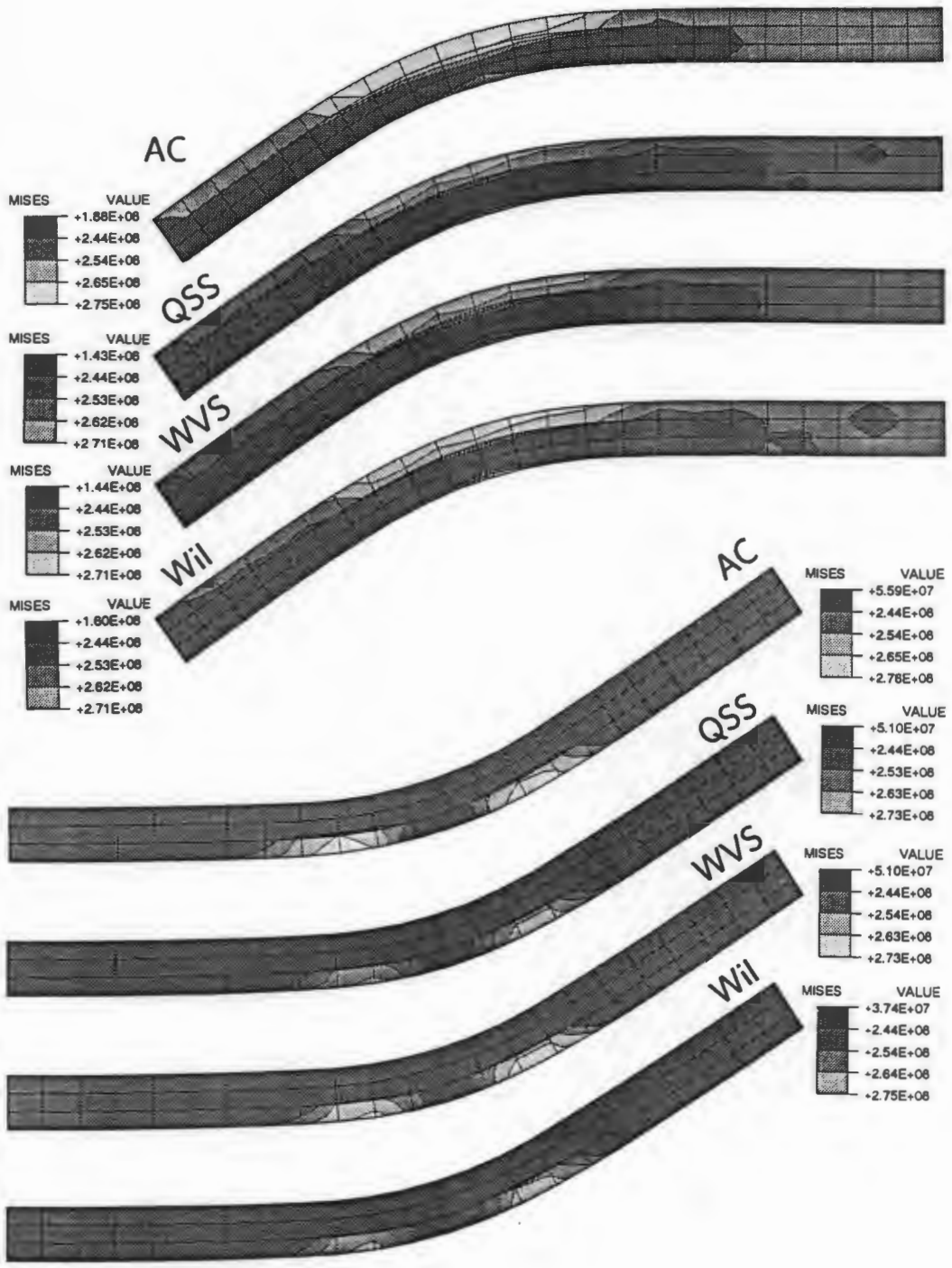

Figure 4.17: The plastic yield stress contour for the axisymmetric cup deep drawing process for the four friction models. Only the flange of the cup is shown, which is divided into the lower bend under the punch (lower set) and the upper bend over the die (upper set).

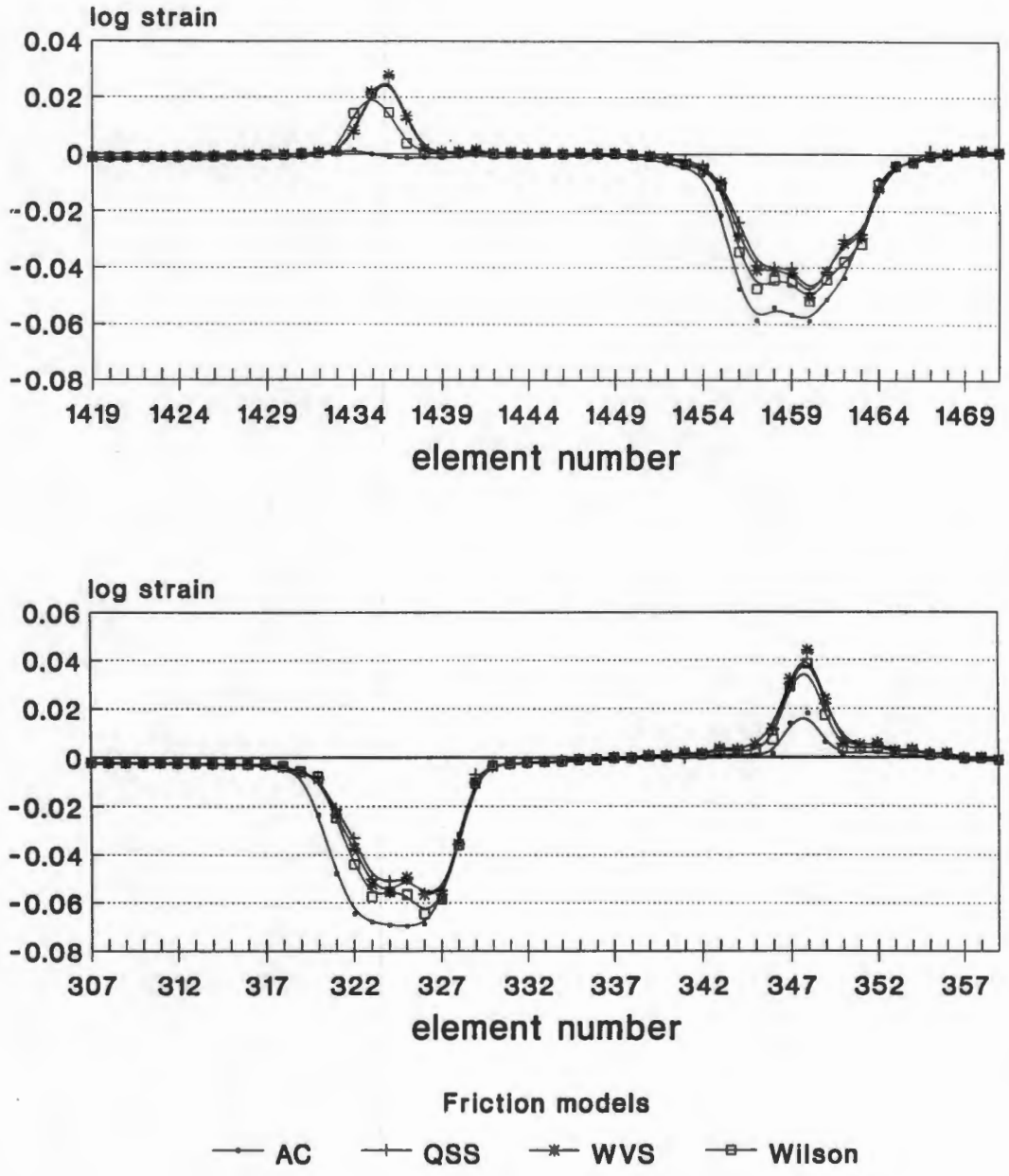

Figure 4.18: Thickness strain ε_{zz} curves for the axisymmetric cup deep-drawing simulation. The values are logarithmic strain for the flange of the cup. The upper graph shows the upper layer, and the lower graph shows the lower layer of elements.

		S_{xx}	S_{yy}	S_{zz}
Wilson	max	314.4	10.77	210.0
	min	−67.2	−58.25	−306.5
AC	max	317.3	28.27	181.6
	min	−64.7	−53.91	−327.7

Table 4.3: The maximum and minimum values of the principle stresses (in MPa) for the deep drawing simulation.

More information can be obtained from the graphs of the thickness strains in figure 4.18. The strip was modelled by three layers of elements, and so the thickness strains for the upper and lower layers are given. The graphs for the four friction models are superimposed to indicate the variations. It can be seen that the extrema show the most variation between friction models. The positions and heights vary.

The peak near elements 1435–1437 occurs at the edge of the punch. As this is mostly a high pressure area we expect the pattern of stick for the friction models to influence the results. The peak occurs at the sticking point, and we can see that the AC model has remarkably little stick compared to the other models. The Wilson model is lower than the QSS and WVS models. We expect the lubrication to reduce the stick, however, the fact that pressure is high at the punch edge and that this is an inlet zone, means that lubricant height is rapidly reduced as lubricant is squeezed out. For the QSS and WVS models, the dry friction is high.

The second peak in the upper layer at elements 1456–1460 occurs outside the blankholder. The high negative strain is mostly due to the reduction in blank thickness caused by bending. The character of the peaks is different for the friction models. The AC is lowest, suggesting less frictional stress, hence less slip, hence more thinning. Similarly for the Wilson model. The two dry models QSS and WVS show less thinning, possibly as the frictional stress was higher, which restricted movement.

In the lower layer, the inverse occurs. The peak at elements 323–326 occurs at the punch edge. The high negative strain is due to thinning caused by bending.

The friction at the punch has effected this to some degree.

Greater difference can be seen at the peak at elements 347–349. This occurs at the edge of the die, where contact occurs under high pressure and we expect higher frictional stress and sticking. The AC model show least strain, suggesting low stress and a small sticking region. Of the other three models the Wilson model is least, but higher than AC. We expect it to be less than the others as the lubricant would reduce friction, but because of the high pressure the lubricant would be very thin, hence the higher value of stress. The two dry models QSS and WVS are very similar, and higher then AC and Wilson.

All this suggests that for deep drawing the AC model, even with a carefully measured coefficient of friction, is inappropriate as the more realistic models, Wilson, QSS and WVS, which account for the greater variation in friction experience over pressure varaition, and especially for the different states of stick and slip, were all similar. Clearly, during steady-state contact the AC model is the worst as it allows little slip. The other models permit a greater amount of movement and so make a big difference to the strains. For the situation where all models allow movement, in a state of slip, there is little difference between models.

Chapter 5

Conclusions

The main achivements of this research are:

1. The comparison of four friction models of different nature.
2. The modelling of three metal forming processes:
   (a) punching, which is a static process;
   (b) rolling, which is a kinematic process; and
   (c) deep drawing, which is quasi-static.
3. The investigation of the applicability of various friction models to the metal forming processes.
4. The comparison of numerical results for each process and friction model.

To accomplish this, each friction model algorithm was implemented in ABAQUS. Mises stress and plastic yield contours, and thickness strains were presented for each combination of process and friction model.

5.1 Friction Models

The four models which have been considered in this paper to model the interaction between a deformed metal and a tool are all different in nature. The classic AC model has a linear relation between pressure and frictional stress. The WVS model uses two impirical relationships to develop a non-linear pressure-dependent relation to replace the AC linear form. The QSS model proposes different frictional stresses for the slipping state and for the sticking state. These dry models were implemented within the FEM using a variant of the "plasticity" theory of friction. This was described in detail in chapter 2. The Wilson model considers a fluid lubricant and roughness effects and uses an equation for the state of the thickness and pressure of the lubricant. Examining the thickness of the lubricant relative to the roughness, the model differentiates between states of full or partial lubrication. For the various regimes of lubrication the frictional stress is calculated from expressions which are derived from micromechanical considerations. The reviewed friction models have been presented in a sequence from a simple model to more advanced models implementing physical phenomena of surface interactions. The more sophisticated models include take into account more physical phenomena giving rise to more complex algorithms which are more expensive to calculate. The computational cost of the models is summerized in the following table:

		AC	QSS	WVS	Wilson
Punching	increments	1.0	1.03	1.17	1.27
	cpu time	1.0	1.17	1.19	1.54
2D rolling	increments	1.0	1.09	1.49	
	cpu time	1.0	1.03	1.52	
3D rolling	increments	1.0	2.54	2.82	
	cpu time	1.0	2.37	3.26	
Deep drawing	increments	1.0	1.19	1.21	1.31
	cpu time	1.0	1.25	1.32	1.33

The table shows the cost of computing relative to the AC model results, which are set to 1.0. The more advanced models require more increments, and are more expensive in cpu time. The Wilson model, in particular, is much more

expensive in computing time. The 3D rolling, with its many degrees of freedom, is the most expensive process. It is thus better to use the AC model, as the results did not differ much.

The parameters for the friction models were chosen so as to represent the same surface characteristics, and to ensure that the rate of dissipation energy is constant. The convergence of the new dry models were typically higher than that for AC under the FEM program ABAQUS. This is due to the nonlinear nature of these models and the slower convergence of the FEM equations. The Wilson model was much slower, and this was due to the extra step which solved the equations for the lubricant. This used a Runga-Kutta routine which naturally required several increments to converge. The accuracy of the results was not extensively investigated as there was not time to calculate the many simulations needed, and there was a lack of consistent and uniform experimental data. Recently this has changed as the report of [31] and the conference proceedings of [29, 22]) are now available to us.

5.2 Results

The processes chosen reflect the standard benchmark processes of metal forming: punching (from forging), rolling (2D plane strain and 3D) and deep drawing of an axisymmetric cup. These processes have been extensively studied in experiment and simulation. A qualitative analysis of the results from the different friction and process simulations was given.

In punching it was found that the WVS model allowed much more slip than the other models. Otherwise, the Wilson model showed more slip than AC and QSS, which were very similar. For this process, it is likely that the differences between AC and QSS are negligible, and that the WVS model was inaccurate as the parameters used were inappropriate. The WVS stress was 12% higher than AC, by contrast the Wilson model only had a stress 1% higher than QSS. The Wilson model behaved as expected: the lubricant allowing more slip, but still similar to the AC and QSS models. Hence, one could use the AC model in this process.

The 3D rolling results were very similar for all three models. The stresses between the AC and QSS models only differ by about 1%, while the stresses between the AC and WVS models differ by about 4%. It would require careful comparison with experiment to chose among them. The plane strain rolling results showed more variation between friction models. The QSS model maximum stress was 20% higher than the AC model, while the WVS model differed from the QSS model by only 0.2%.

In deep drawing there were large differences in the strain graphs. The QSS model allowing more slip, which is closer to what is expected. The AC model seemed quite bad for the areas where the blank is sticking, and so should perhaps be not used. The Wilson model show the best result, and it should be considered for this simulation. The WVS model had greater stresses and sticking, and so indicates how deep drawing without any lubricant would behave, with great thinning and wrinkling. As deep drawing is always performed with a lubricant, the dry models should be dropped in favour of Wilson. However, as the region under the punch is always sticking, and the lubricant is very thin, it may be preferrable to use a dry model, which is less expensive, under the punch, and use the Wilson model between blankholder, blank and die. The maximum stresses for the QSS and WVS models are identical, and the AC and Wilson model only differ by about 1% at most.

5.3 Further Research

The work presented here can be broadened and continued in many ways. Briefly, aspects that should be considered for the developement and implementation of new friction models are mentioned below:

Investigation of the sensitivity of the friction models to variation in the parameters would be necessary. Especially, the sensitivity of the friction stresses to pressures, as this would indicate in a clear manner how a model would influence the solution of a simulation. Further, work need to be peformed on the convergence of the FEM using these models. The variation in solution times indicates that some models may be inappropriate because thay are too expensive. Hence, the algorithms need to be optimised to work efficiently.

The interaction and connection between the friction model and the material model should be investigated. In order to accurately model a real situation it seems preferable that a friction model be compatible with the material reaction at the surface, e.g., viscous effects in the body require a friction model sensitive to the velocity of relative surface motion. This paper has used an elastic-plastic material with a plastic approach to the friction. For other materials, e.g., viscoplasticity, another friction model might be appropriate, which takes into account the velocity of surface tangential displacement.

Consideration of thermal effects have been neglected in this paper. There can be considerable dissipation of energy from frictional sliding, which is converted into heat, and this would be transferred to the contacting bodies. The heat would affect the parameters of the friction and material functions. Also, abrasion, wear and tear continually change the characteristics, especially the topology, of a surface. This would influence the friction, as mentioned in chapter 1.

In this last regard, more attention needs to be focussed on modelling real surfaces: the topology, material parameters and behavour. A promising approach is to treat surfaces and friction in a stochastic framework. This opens the possibility of reducing the many micromechanical effects to a single quantity of average tangental resistance or surface "stiffness".

Bibliography

[1] B. AVITZUR, *Handbook of Metal-Forming Processes.* (New York, NY: John Wiley & Sons) 1983.

[2] K-J. BATHE, *Finite Element Procedures in Engineering Analysis.* (Englewood Cliffs, NJ: Prentice-Hall) 1982.

[3] F.P. BOWDEN & D. TABOR. *The Friction and Lubrication of Solids, Part I.* (London: Oxford University Press) 1950.

[4] F.P. BOWDEN & D. TABOR. *The Friction and Lubrication of Solids, Part II.* (London: Oxford University Press) 1964.

[5] F.P. BOWDEN & D. TABOR, *Friction and Lubrication.* (London: Methuen) 1967.

[6] R. BUCZKOWSKI & M. KLIEBER, Finite element analysis of elastic-plastic plane contact problem with nonlinear interface complience. *Journal of Theoretical and Applied Mechanics* **30**(4) (1992) 855–883.

[7] A. CAMERON, *Basic Lubrication Theory,* third edition. (Chichester: Ellis Horwood) 1981.

[8] H. CHRISTENSEN, Stochastic models for hydrodynamic lubrication of rough surfaces. *Proceedings of the Institute of Mechanical Engineers* **104** 1 (1970) 1013–1022.

[9] A. CURNIER, A theory of friction. *International Journal of Solids and Structures* **20**(7) (1984) 637–647.

[10] E.A. DE SOUZA NETO, K. HASHIMOTO, D. PERIC & D.R.J. OWEN, A phenomenological model for frictional contact of coated steel sheets. Presented at NUMISHEET93, the Second International Conference on Numerical Simulation of 3-D Sheet Metal Forming Processes, Isehara, Japan, 31 August – 2 September 1993.

[11] D.D. FULLER, Friction. In: T. Baumeister, E.A. Avallone & T. Baumeister III (eds.), *Mark's Standard Handbook for Mechanical Engineers,* 8th edition. (New York, NY: McGraw-Hill) 1978.

[12] P. HEILMANN & D.A. RIGNEY, An energy-based model of friction and its application to coated systems. *Wear* **72** (1981) 195–217.

[13] N. KIKUCHI & J.T. ODEN, *Contact Problems in Elasticity: A Study of Variational Inequalities and Finite Element Methods.* SIAM Studies in Applied Mathematics 8 (Philadelphia: SIAM) 1988.

[14] I.V. KRAGELSKY, M.N. DOBYCHIN & V.S. KOMBALOV, *Friction and Wear: calculation methods.* Translated from the Russian by N.S. Standen (Oxford: Pergamon Press) 1982.

[15] S.M. MAHDAVIAN & Z.M. SHAO, Isoviscous hydrodynamic lubrication of deep drawing and its comparison with experiment. *Journal of Tribology* **115** (1993) 111–118.

[16] J.T. ODEN & E.B. PIRES, Nonlocal and nonlinear friction laws and variational principles for contact problems in elasticity. *Journal of Applied Mechanics* **50** (1983) 67–76.

[17] J.T. ODEN & E.B. PIRES, Numerical analysis of certain contact problems in elasticity with non-classical friction laws. *Computers & Structures* **16** (1983) 481–485.

[18] J.T. ODEN & E.B. PIRES, Algorithms and numerical results for finite element approximations of contact problems with non-classical friction laws. *Computers & Structures* **19** (1984) 137–147.

[19] N. PATIR & H.S. CHENG, An average flow model for determining effects of three-dimensional roughness on partial hydrodynamic lubrication. *Journal of Lubrication Technology* **100** (1978) 12–17.

[20] N. PATIR & H.S. CHENG, Application of an average flow model to lubrication between rough sliding surfaces. *Journal of Lubrication Technology* **101** (1979) 220–230.

[21] D. PERIC & D.R.J. OWEN, Computational model for 3-D contact problems with friction based on the penalty method. *International Journal for Numerical Methods in Engineering* **35** (1992) 1289–1309.

[22] D. PERIC, D.R.J. OWEN, M. SCHONAUER & E.A. DE SOUZA NETO, Computaional strategies for finite strain plasticity problems including adaptivity concepts. Presented at FEMSA93, the Twelfth Symposium on Finite Elements in South Africa, University of Pretoria, 7–9 July 1993.

[23] T. RODIC & D.R.J. OWEN, A plasticity theory of friction and joint elements. In: *Computational Plasticity: Fundamentals and Applications* [Proceedings of the second international conference held in Barcelona, Spain.] (Swansea, U.K.: Pineridge Press) 1989.

[24] J. RONDA, O. MAHRENHOLTZ, M. BRZOZOWSKI & R. BOGACZ, The rolling contact problem for an elastic-plastic strip and a rigid roller. *Mechanics Research Communications* **13** (1986) 119–132.

[25] J. RONDA, Friction in nonstationary contact problems. (In Polish). Habilatation thesis, Reports of the Institute of Fundamental Technology 1/1990 (Warsaw: IPPT PAN) 1990.

[26] J. RONDA, R. BOGACZ & M. BRZOZOWSKI, Infinitesimal and large strain in rolling contact problems. *Ingenier-Archiv* **56** (1986) 241–253.

[27] J. RONDA & K.W. COLVILLE, Influence of friction models on nonstationary contact problems solution. In: *Computational Plasticity: Fundamentals and Applications,* [Proceedings of the third international conference held in Barcelona, Spain.] (Swansea, U.K.: Pineridge Press) 1993.

[28] J. RONDA & K.W. COLVILLE, Modelling of friction phenomena in plastic working. Presented at FEMSA93, the Twelfth Symposium on Finite Elements in South Africa, University of Pretoria, 7–9 July 1993.

[29] J. RONDA, C.D. MERCER, A.S. BOTHMA, G.J. OLIVER & K.W. COLVILLE, Simulation of square cup deep drawing with various

friction and material models. Presented at NUMISHEET93, the Second International Conference on Numerical Simulation of 3-D Sheet Metal Forming Processes, Isehara, Japan, 31 August – 2 September 1993.

[30] J.A. SCHEY, *Tribology in Metalworking: Friction, Lubrication and Wear.* (Metals Park, OH: American Society for Metals) 1983.

[31] W. SOSNOWSKI, E. OÑATE & C. AGELET DE SARACIBAR, *Numerical Simulation of Industrial Sheet Forming Processes, Part I: Description of the Experiments.* International Center for Numerical Methods in Engineering, Barcelona, Spain. Technical report, May 1992.

[32] D. TABOR, Friction, surface science and tribology—a personal view. *Journal of Mechanical Engineering Science* **205** (1991) 365–378.

[33] J.H. TRIP, Surface roughness effects in hydrodynamic lubrication: the flow factor method. *Journal of Lubrication Technology* **101** (1983) 458–465.

[34] W.R.D WILSON, Friction models for metalforming in the boundary lubrication regime. *Journal of Engineering Materials and Technology* **113** 1 (1991) 60–68.

[35] W.R.D WILSON, Mixed lubrication in metal forming. In: *Advanced Technology of Plasticity 1990,* volume 4. (Japanese Society of Technical Plasticity) 1990, pp1667–1675.

[36] W.R.D. WILSON, T.C. HSU & X.B. HUANG, A realistic friction model for computer simulation of sheet metal forming processes. Unpublished preprint (1992).

[37] W.R.D. WILSON & S. SHEU, Real area of contact and boundary friction in metal forming. *International Journal of Mechanical Sciences* **30** (1988) 475–489.

[38] W.R.D. WILSON & J.J. WANG, Hydrodynamic lubrication in simple stretch forming processes. *Journal of Tribology* **106** (1984) 70–77.

[39] K.L. WOO & T.R. THOMAS, Contact of rough surfaces: a review of experimental works. *Wear* **58** (1980) 331–340.

[40] P. WRIGGERS, T. VU VAN & E. STEIN, Finite element formulation of large deformation impact-contact problems with friction. *Computers & Structures* **37** 3 (1990) 319–331.

[41] J. ZHANG, F.A. MOSLEHY & S.L. RICE, A model for friction in quasi-steady-state sliding. Part I: Derivation. *Wear* **149** (1991) 1–12.

[42] J. ZHANG, F.A. MOSLEHY & S.L. RICE, A model for friction in quasi-steady-state sliding. Part II: Numerical results and discussion. *Wear* **149** (1991) 13–25.